Direct collapse black hole formation and assembly in cosmological simulations

By

Glenna Caitlin Dunn

Dissertation

Submitted to the Faculty of the

Graduate School of Vanderbilt University

in partial fulfillment of the requirements

for the degree of

DOCTOR OF PHILOSOPHY

in

Astrophysics

August 9, 2019

Nashville, Tennessee

Approved:

Kelly Holley-Bockelmann, Ph.D.

Andreas Berlind, Ph.D.

David Weintraub, Ph.D.

Jillian Bellovary, Ph.D.

William French, Ph.D.

For my family, given and chosen.

ACKNOWLEDGMENTS

None of this would have been possible without the academic and emotional support of so many people.

First, I must thank the mega-brain, my advisors Kelly Holley-Bockelmann and Jillian Bellovary, for their years of unwavering support. Kelly and Jillian believed in me from the first time we met, long before I believed I could do this work myself. I thank Charlotte Christensen and Tom Quinn for patiently sharing their insight into the intricacies of Gasoline and ChaNGa, which were absolutely vital to my success. I thank Jon, Jedidah, Duane, Lauren, and Victor for helping me prepare for my qualifying exam. I thank the women of the N-body group for making me feel welcome in their space. I thank my friends at Vanderbilt for making graduate school just a little bit easier, especially Gillian, who I consider a kindred spirit, and Adam, who has more than once made me laugh so hard I fell out of my chair in tears. I thank my Mom for always valuing my education, especially when I did not yet see its importance. I thank my sisters for their camaraderie as we all went through graduate school together. Most of all, I thank Zoë for joining me on this adventure, keeping me grounded, and making Nashville our home.

TABLE OF CONTENTS

LIST OF TABLES

Table Page

LIST OF FIGURES

Figure Page

Chapter 1

Introduction

For several decades now, observations of our own galaxy and others near and far demonstrate that massive black holes live at the centers of most massive galaxies (Ghez et al., 2005; Kormendy & Richstone, 1995; Kormendy & Ho, 2013). Particularly, the discovery of luminous quasars at redshift $z = 6$ and beyond has prompted the question of how black holes could form and grow to masses in excess of $10^6\ M_\odot$, and reaching up to $10^9\ M_\odot$, within the first billion years of the Universe. The origin of these black holes is the subject of much debate.

In this Thesis, I discuss efforts to better understand the formation and mass assembly of massive black holes (MBHs) through cosmological N-body smoothed particle hydrodynamic simulations of a Milky Way-type galaxy. The purpose of this work is three-fold. Firstly, I develop an improved model of massive black hole seed formation that reflects Lyman-Werner driven direct collapse. This is the first work to self-consistently model direct collapse black hole formation in a cosmological context with a temporally and spatially varying Lyman-Werner radiation field. Secondly, I employ this model to study the conditions of MBH formation. In contrast with the canonical model for the formation of the first balck holes, I find that multiple direct collapse black hole seeds can form in halos with recent nearby star formation. Finally, I use the results of my study of MBH formation sites to explore the early assembly of MBH seeds through black hole mergers. This work highlights that mergers and ejections due to gravitational recoil are likely important to early MBH-host co-evolution, and demonstrates the importance of incorporating the physics and black hole mergers into models that make predictions about observable signatures of massive black hole seeds.

1.1 Black holes and their hosts

Most, if not all, galaxies with spheroidal components host super-massive black holes (SMBHs) at their centers, and these objects are thought to co-evolve with their hosts. The effect of a central black hole is apparent throughout the host galaxy on scales larger that the black hole itself. Feedback from active galactic nuclei (AGN) powered by SMBHs can regulate star formation in a host galaxy through ionization, heating, and kinetic feedback (e.g., Di Matteo et al., 2005; Harrison, 2017). Gas-rich galaxy mergers feed the growth of an central black hole (e.g., Debuhr et al., 2011; Capelo et al., 2015; Goulding et al., 2018), and in turn feedback from the accreting black hole self-regulates its own growth (e.g., Wyithe & Loeb, 2003; Treister et al., 2011; Dubois et al., 2012a; Aykutalp et al., 2014; Hartwig et al., 2018). SMBH feedback can even change the shape of the host galaxy's dark matter density profile (e.g., Governato et al., 2010; Peirani et al., 2017).

Several empirical relations demonstrate that the mass of a central black hole is tied to observable properties of the spheroidal component of its host galaxy. An abundance of observations have shown that the spheroidal velocity dispersion ((Ferrarese & Merritt, 2000; Gebhardt et al., 2000) also see (Gültekin et al., 2009; McConnell & Ma, 2013) for a review), bulge mass (Magorrian et al., 1998; Häring & Rix, 2004) and bulge luminosity (Kim et al., 2008) of the host galaxy all scale with the mass of the black hole at its center. Figure 1.1, selected from McConnell & Ma (2013) shows the $M - \sigma$ relation as derived from a collection direct dynamical black hole mass measurements. Additional work extends these established relationships to include the galaxies that host nuclear star clusters (Ferrarese et al., 2006; Graham, 2012), barred spirals (Graham et al., 2011), and pseudo-bulges (Graham, 2008). The influence of a central black hole is even linked to the number (Harris & Harris, 2011; Harris et al., 2014) and velocity dispersion (Sadoun & Colin, 2012) of globular clusters

observed in a host galaxy. These scaling relations provide convincing evidence that the formation and evolution of black holes and their host galaxies are closely linked.

These different scaling relations likely point to the role of different modes of black hole feedback in the global evolution of a host galaxy (Kormendy & Ho, 2013). However, the origin and magnitude of the scatter in these relations is not yet well understood (Gültekin et al., 2009). The $M-\sigma$ and $M_{BH}-L_{bulge}$ relations in particular suffer from selection bias that favor brighter, more massive systems (Bernardi et al., 2007; Gültekin et al., 2009). While these relationships seem well-established for higher-mass systems, there remains a question as to its relevance for lower-mass or higher-redshift systems (Zhu et al., 2012). The clear connection between an SMBH and its host only compounds the need to better understand the physics of SMBH formation and early growth. There are still several unknowns regarding these scaling relations between an SMBH and its host. Are they in place at the time of formation, or does a black hole-galaxy pair evolve onto these relations over cosmic time? Do these scaling relations hold for galaxies of all masses, or do they break down for low-mass systems? Observations at high redshift are particularly crucial for understanding the origin of these scaling relations.

1.2 Observational evidence of black holes

Supermassive black holes with masses $10^6-10^9 M_\odot$ are found at the centers of most massive galaxies (Kormendy & Richstone, 1995). A variety of techniques are employed to constrain the presences of black holes in host galaxies. Detection methods vary with the the distance, line-of-sight inclination, accretion rate, and host environment of a black hole.

Direct measurements of black hole masses rely on the spatially-resolved observations of kinematics of stars or gas orbiting the black hole. The mass of the supermassive black hole at the center of our own Milky Way galaxy, Sagittarius A*, was determined through

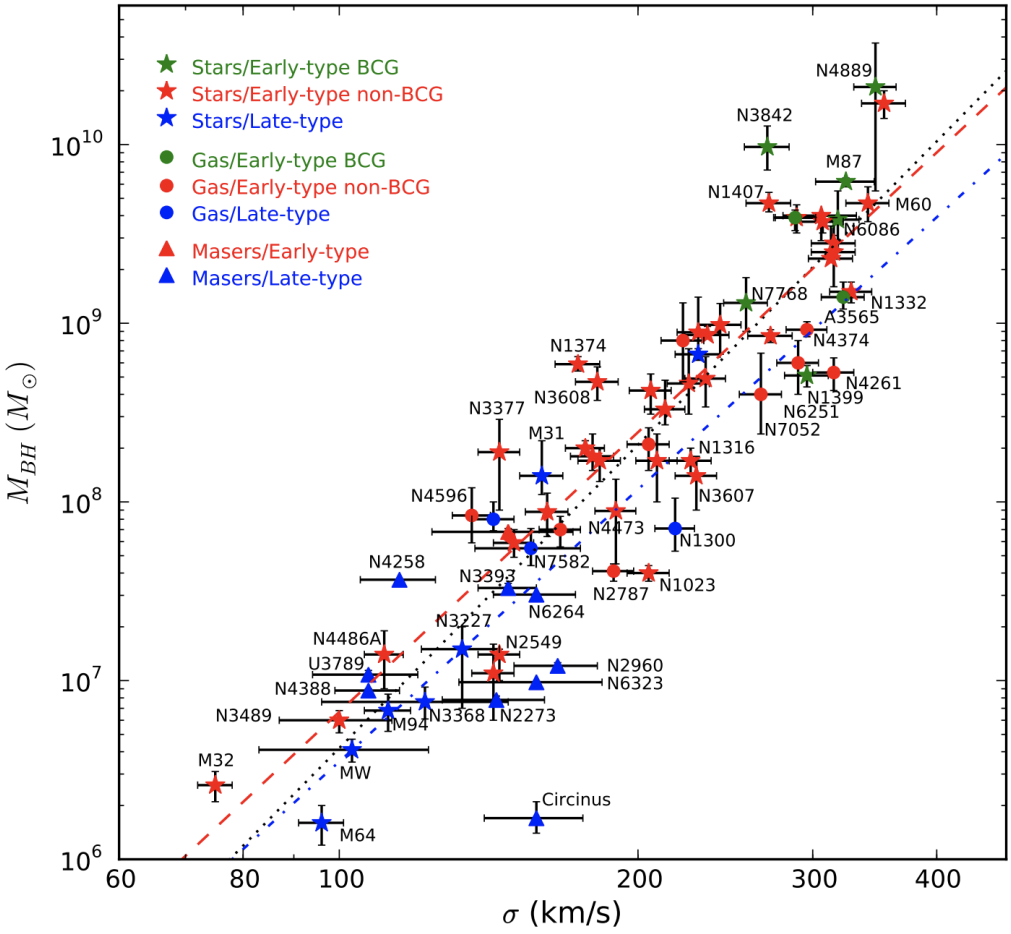

Figure 1.1: THE $M-\sigma$ RELATION This figure, selected from McConnell & Ma (2013), shows $M-\sigma$ value pairs for a sample of 72 black hole-galaxy pairs. Central galaxies are marked in green, non-central elliptical and S0 galaxies are marked in red, and spiral galaxies are marked in blue. Error bars represent 3σ confidence intervals. The error bars on black hole mass measurements for the sample of masers are often smaller than the marker size. Note that the fit for early-type and brightest cluster galaxies predicts larger black hole masses for all values of velocity dispersion in the measured range than the fit for late-type galaxies.

resolved stellar dynamics. Years of infrared imaging of the Galactic center revealed that stars in this region orbit the same point with highly eccentric, short-period Keplerian orbits (Ghez et al., 2005; Meyer et al., 2012). This technique is only available to the most nearby systems, as the orbits of the stars orbiting distant objects are not resolved.

In rare circumstances, such as the edge-on galaxy NGC 4258 (Greenhill et al., 1995; Miyoshi et al., 1995; Bragg et al., 2000) the presence of a black hole is inferred from the observation of orbiting gas clouds near the center of a galaxy. These objects, known as masers, are characterized by stimulated emission lines detected in the radio band. These emission lines are generated by feedback from an accreting black hole that provides enough energy to pump molecules, typically H_2O, in an orbiting gas cloud into an excited energy state. Doppler shift measurements of these emission lines reveal the orbital velocity of a maser cloud, and thereby the mass of the object it orbits.

Reverberation mapping is a technique used to measure the size of the broad-line region around an AGN. Reverberation mapping tracks the response of the broad-line emission region of an actively accreting AGN to variations in the luminosity of the accretion disk, which acts as a continuum source. As material accretes onto the black hole, gravitational potential energy is converted into radiation. Light from the broad-line emission region is re-processed by the accretion disk; measurements of the time delay the variable broad-line emission and the continuum reveal the distance between the broad line region and the central black hole. This calculated distance, paired with additional measurements of the Doppler broadening of the emission lines that are used to calculate the velocity dispersion of the broad line region, provide an estimate of the mass of the central black hole:

$$M_{BH} = f\frac{r\delta v_r}{G} \tag{1.1}$$

Reverberation mapping trades the spatial resolution of direct measurements for time resolution, making it more time intensive than other SMBH mass measurement techniques.

One serious drawback of reverberation mapping is its dependence on the geometry and kinematics of the broad line region, which not yet well understood. This uncertainty is represented by a poorly-constrained scaling factor f of order unity. Reverberation mapping also relies on an empirical relationship between the size of the broad line region and the AGN continuum luminosity, because the broad line region in unresolved (Kaspi et al., 2000). Despite these caveats, reverberation mapping is a popular method for determining black hole masses, and is currently employed to estimate black hole masses for hundreds of high-redshift quasars in the Sloan Digital Sky Survey (Grier et al., 2019).

1.3 Black hole formation

The detection of quasars, super-massive black holes with masses $\sim 10^6 - 10^9 M_\odot$, at redshifts $z = 6$ and beyond pose the question of how these objects assembled their mass so quickly. Two unsolved problems related to massive black hole formation are the questions of the number density and initial mass of the massive black hole seed. Presently, three major theories describe possible massive black hole seed formation pathways. Each black hole seed formation model suggests different seed mass distributions and number densities, hinting that they may be observationally differentiable. All of these formation pathways begin with collapsing over-densities of gas at high redshift. Where they diverge is in the state of the gas as it collapses: does the gas fragment as it collapses, or does it collapse monolithically? These formation mechanisms are not mutually exclusive, and it is entirely possible that more than one of these pathways contribute to the total population of massive black hole seeds.

One possibility is that massive black hole seeds are the remnant of Population III stars (e.g., Madau & Rees, 2001; Haiman & Loeb, 2001; Tanaka & Haiman, 2009). This formation pathway mirrors the familiar formation mechanism of stellar-mass black holes in the local

Universe. The number and mass of these seeds would depends strongly on the initial mass function of Population III stars, which is not currently well-constrained. It is generally accepted though that Population III stellar remnants would yield lower-mass seed black holes, but these seeds would be plentiful, and found in most halos. The first stars formed in mini-halos with virial temperatures $\sim 10^3$K (and virial masses $10^5 - 10^6 M_\odot$), which allow gas to cool and fragment by forming molecular Hydrogen. While early work indicated that Population III stars formed with masses $\sim 10^2 - 10^3 M_\odot$ (e.g., Bromm et al., 2002; Abel et al., 2002), later simulations showed that disk fragmentation yields stellar masses closer to $10 - 10^2 M_\odot$ (e.g., Stacy et al., 2010; Hartwig et al., 2015; Stacy et al., 2016). These Population III remnants would likely form with masses $\sim 10 M_\odot$, and therefore would need to grow by several orders of magnitude in order to reach quasar-like masses. This would require some combination of sustained accretion at or above the Eddington limit for spherical accretion and multiple mergers to grow these seeds to masses observed during the quasar epoch. The combination of a limited gas reservoir and feedback from the accreting black hole makes sustained Eddington-limited accretion unlikely (Alvarez et al., 2009; Aykutalp et al., 2014).

Alternatively, it is possible that these seeds form not from a single star, but rather runaway stellar collisions in dense nuclear star clusters (e.g., Begelman & Rees, 1978; Devecchi & Volonteri, 2009; Katz et al., 2015; Sakurai et al., 2017). These clusters form in low-metallicity atomic cooling halos ($T_{vir} > 10^4$K) slightly after the formation fo the first stars, with masses $\sim 10^5 M_\odot$ (e.g., Devecchi & Volonteri, 2009). Runaway collisions form a very massive star that evolves to yield a massive black hole seed. Low metallicity environments are favored for this process because mass loss to to stellar winds of solar metallicity stars greatly suppresses the final black hole mass (Mapelli, 2016). The massive black hole seeds would form at redshifts $z \sim 10 - 20$ with masses $\sim 10^3\ M_\odot$. If the cluster experiences core collapse, fast mergers angular momentum transport of gas from the cosmic web to the collapsing core can yield a black hole a mass of $\sim 10^5 M_\odot$ (Davies et al., 2011).

Finally, a third theory suggests that, under particular conditions only present in the early Universe, gas can collapse directly massive black hole seeds without ever forming stars. In this *direct collapse* theory, gas in pristine pre-galactic halos might form black hole seeds as large as $10^4 - 10^6 M_\odot$ (e.g., Loeb & Rasio, 1994; Begelman et al., 2006, 2008; Begelman, 2010; Shang et al., 2010; Yue et al., 2014, 2017). Such direct collapse black holes are expected to be quite rare, as the gas must collapse without fragmentation so as to bypass star formation completely. Additionally, the inflow rate of the collapsing region must reach $0.1 - 1\ M_\odot$/yr for $\sim 10^6$ yr (Begelman, 2010; Hosokawa et al., 2013; Schleicher et al., 2013; Latif et al., 2015). Low angular momentum halos subject to global instability are favored as environments conducive to direct collapse (Begelman et al., 2006; Begelman & Shlosman, 2009). These halos must also be metal-free and subject to strong radiation in the Lyman-Werner band to prevent the formation of molecular Hydrogen (Visbal et al., 2014a,b; Latif et al., 2014, 2015, 2016; Regan et al., 2017; Agarwal et al., 2014). As the gas accumulates and collapses, it may form a single supermassive star that yields a massive black hole seed (Wise et al., 2019), or a quasi-star with a central black hole that accretes the outer stellar envelope (Begelman et al., 2006; Volonteri, 2010; Schleicher et al., 2013). Regardless of the exact physics, the direct collapse process would likely yield high-mass black hole seeds, but these seeds would be rare. The theory of direct collapse is the subject of Chapter 2, and discussed in more detail there.

1.4 Black hole growth: accretion and mergers

The two modes of black hole growth are gas accretion and mergers with other black holes. Accretion occurs when material is gravitationally attracted to a compact object, such as a black hole. Black hole accretion rates are limited by self-regulating feedback and the mass of the gas reservoir available for accretion. Accretion likely occurs in disks, and is

not bound by the spherically-symmetric Eddington limit. Such accretion disks are likely sub-parsec in size, and therefore well below the resolution limits of our simulations.

The Bondi-Hoyle accretion model describes spherical accretion onto a point mass:

$$\dot{M}_{BH} = \frac{4\pi\alpha G^2 M_{BH}^2 \rho}{(c_s^2 + v^2)^{3/2}} \tag{1.2}$$

in which M_{BH} is the mass of the black hole, ρ is the density of the surrounding gas, c_s is the speed of sound ing the gas, and v is the relative velocity between the black hole and the surrounding medium. The parameter α moderates the accretion rate, and is set to unity in this work. While the assumption of spherical accretion is an idealized model, it is appropriate for simulations such those discussed in this work, in which the force resolution is on the order of hundreds of parsecs and black holes are treated as Newtonian point masses. Spherically symmetric accretion is limited by the Eddington rate: the maximum possible rate of spherical accretion onto a compact object is balanced by radiation pressure from the energy released by the accreting gas. An accretion disk, which is not bound by spherical symmetry and is a more realistic representation of the sub-parsec accretion physics, can allow black holes to accrete at super-Eddington rates. The accretion disk has been invoked as a possible solution to the question of rapid SMBH growth in the pre-quasar epoch in both simulations (e.g., Pezzulli et al., 2016) and observations (e.g., Tang et al., 2019).

Accretion in our simulations is modeled as spherically symmetric Eddington-limited Bondi-Hoyle accretion, which reasonably reproduces accretion at the $\sim$kpc scales we can resolve. A more realistic picture of black hole accretion would model the accretion disk around the compact object, but a simulation with resolution of hundreds of parsecs cannot reliably describe accretion events that happen on the scale of an AU (Volonteri & Bellovary, 2012). Furthermore, these simulations rely on sub-grid physics models to approximate the composition of the gas because they cannot fully describe the multi-phase interstellar medium. This can lead to a chronic underestimation of gas density, whereas it is the densest

gas that should accrete most easily onto the black hole. If the gas density is underestimated at the accretion radius due to resolution effects, the Bondi-Hoyle accretion rate is artificially suppressed, effectively inhibiting black hole growth in all but the most massive halos. A modified Bondi-Hoyle prescription that allows the black hole to preferentially accrete gas above a threshold density may reproduce accretion in the multi-phase interstellar medium more reliably (Booth & Schaye, 2009).

Black holes can also gather mass through mergers with other black holes. Black hole mergers are typically invoked as a consequence of hierarchical galaxy growth through mergers. These merges likely yield a variety of populations of black holes (e.g., Comerford et al., 2015; Koss et al., 2018). Major mergers between galaxies with similar masses can create dual AGN, in which two accreting black holes form a binary system on $\sim$kpc scales. A similar situation resulting for unequal mass galaxy mergers can create offset AGN, in which only one of the binary black holes accretes. MBH-MBH mergers offer a convenient pathway for rapid black hole seed growth, particularly if MBH seeds can form in a single halo.

When two black holes coalesce, they pass through three phases: inspiral, merger, and ringdown. The inspiral of a binary black hole begins at large separation is characterized by a shrinking orbit, increasing orbital speeds, and increasing gravitational wave emissions. Over the course of millions of years, the binary system experiences a catastrophic cycle of energy and angular momentum loss: the orbiting binary loses energy to gravitational waves, which decreases the orbital distance between the two black holes and increases their orbital speeds and increases the strength of the emitted gravitational waves. Once the black holes cross the innermost stable circular orbit, the merger phase begins, and the two black holes plunge together in a dynamical time to form a merged object that is deformed by the mutual gravitational attraction of the two black holes. Finally, the merged black hole enters the ringdown stage, in which it radiates away energy as gravitational waves as it oscillates and settles into a single stable black hole.

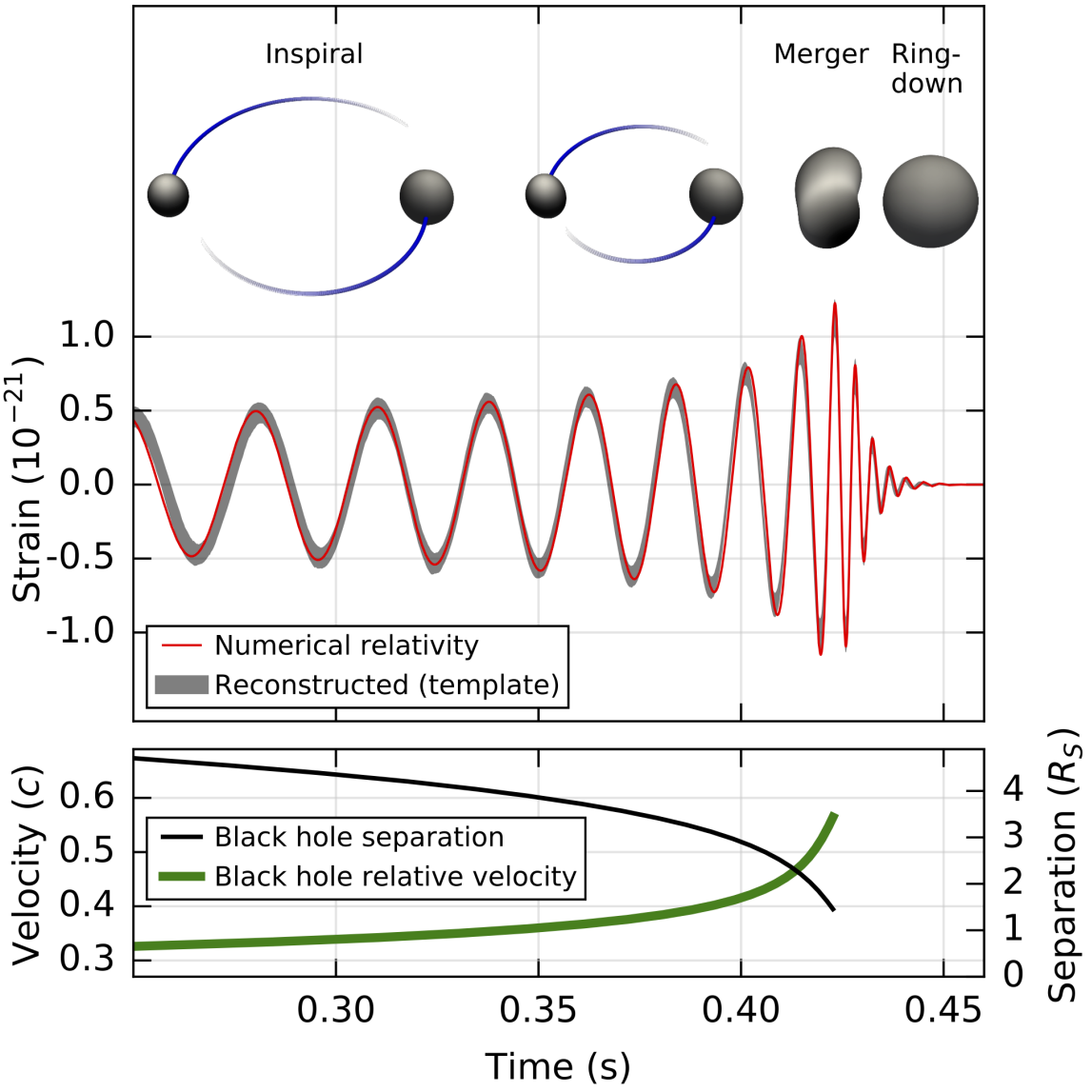

Figure 1.2: GRAVITATIONAL WAVE SINGAL FROM A BINARY BLACK HOLE MERGER GW150914 was the first gravitational wave source detected by the Laser Interferometer Gravitational-Wave Observatory (LIGO). This gravitational wave event was the coalescence of a binary black hole system with masses of $36^{+5}_{-4}M_{\odot}$ and $29^{+4}_{-4}M_{\odot}$ in the $z = 0.09^{+0.03}_{-0.04}$ source frame (Abbott et al., 2016). This figure, selected from Abbott et al. (2016), shows the gravitational wave strain amplitude and relative velocity and separation for this binary black hole merger. In the top panel, a cartoon depicts the three phases of binary black hole coalescence.

In Gasoline, we allow black holes with low relative velocities that are separated by less than two softening lengths to merge. Black hole mergers are the subject of Chapter 3 and discussed in more detail there.

1.5 Black hole feedback

Just as stars modify their surroundings through radiation and supernovae, providing energy to delay and metals to enrich future episodes fo star formation, accreting black holes also transform their local and global environments through feedback. Active galactic nuclei inject energy and momentum into their environments that modifies their host galaxies on distance scales that are orders of magnitude larger than the sub-parsec scales of SMBH accretion physics. Feedback from accreting black holes is an integral part of galaxy evolution, responsible for shutting of gas cooling and redistributing gas in a galaxy. As AGN feedback can redistribute gas through massive outflows, it is also a self-regulating process that limits SMBH growth (e.g., Di Matteo et al., 2005; Sijacki et al., 2007). Feedback is categorized into two modes (Fabian, 2012): quasar mode feedback, associated with high accretion rates and large gas inflows, and radio mode feedback, associated with low accretion rates.

Quasar mode feedback can take the form of winds or radiation, and is usually observed in high-luminosity, high-redshift galaxies. Radiative feedback occurs when a central black hole accretes near the Eddington limit and with high radiative efficiency, and effectively moves cold gas. This mode of feedback is likely responsible for uniform heating of gas throughout the spheroidal bulge, setting the stage for the $M - \sigma$ relation (Fabian, 2012).

Radio mode feedback often takes the form of jets, and is typically found in low-luminosity, low-redshift galaxies, massive ellipticals, or Seyfert galaxies and observed in the X-ray and radio bands (e.g., Okamoto et al., 2008). Radio feedback can moderate or even quench star formation by heating gas. This form of feedback may be responsible for shutting off cooling in massive galaxies.

These two modes of AGN feedback are not mutually exclusive, and while a single mode dominates in the most extreme regimes of high- and low-luminosity AGN, both modes may appear in feedback from AGN accreting at more intermediate levels. While most forms of feedback seem to prevent the cooling of gas, and therefor also prevent star formation, recent work has shown that mass outflows may ignite star formation by compressing gas to sufficiently high densities (e.g., Maiolino et al., 2017). AGN feedback is an important component of SMBH-host galaxy co-evolution, and may contribute to the diversity of galaxy morphologies (e.g., Di Matteo et al., 2008; Dubois et al., 2016).

In the simulations used in this work, a fraction of the rest-mass energy of an accreted gas is converted to thermal (radiative) energy according to Di Matteo et al. (2005), and is distributed isotropically to gas particles near the black hole.

1.6 Primordial gas chemistry

Gas cooling is the process that allows gas to condense to the densities required to ignite star formation. Gas can cool through collisional excitation and ionization, recombination, molecular rotation, or Bremsstrahlung radiation. In the local Universe, gas can cool through atomic Hydrogen, Helium, metal lines, molecular hydrogen, or dust. At the high redshifts of massive black hole seed formation, metal-line cooling is unimportant, as the first generations of stars have yet to pollute their host halos with heavy elements. The most efficient coolant at this time is molecular hydrogen (H_2), which can cool gas with temperatures of 10^4 K down to $\sim 10^2$ K. Molecular hydrogen forms readily on the surface of dust grains, but in the absence of such in the early Universe, H_2 forms via two channels (Glover, 2011), primarily

$$H + e^- \rightarrow H^- + \gamma \tag{1.3}$$

$$H^- + H \rightarrow H_2 + e^- \tag{1.4}$$

and secondarily

$$H_2^+ + H \rightarrow H_2 + H^+. \tag{1.5}$$

Molecular hydrogen is dissociated by Lyman-Werner photons with energies $h\nu = 11.2 - 13.6$ eV:

$$H_2 + \gamma_{LW} \rightarrow H + H \tag{1.6}$$

What amount of radiation is necessary to sufficiently suppress H_2 formation in an atomic cooling halo with $T_{vir} \gtrsim 10^4$ K? This value, J_{crit}, is expressed in units of J_{21}: $J_{21} = 10^{-21} ergs^{-1} cm^{-2} Hz^{-1} sr^{-1}$. Authors have attempted to constrain the value of J_{crit} required for direct collapse (e.g., Haiman et al., 2000; Glover, 2015a; Latif et al., 2015), but these estimates still span several orders of magnitude. One significant source of uncertainty in the value of J_{crit} is the shape of the irradiating spectrum, particularly the hardness of the X-ray radiation (Regan et al., 2016). In this work, we address the uncertainty of J_{crit} with a suite of simulations with different J_{crit} values that span the range presented in the literature.

1.7 Gas collapse and fragmentation

What is the maximum size of a collapsing gas cloud? The Jeans length, which derives from the virial theorem, approximates the scale at which a self-gravitating object collapses:

$$L_J \sim \sqrt{\frac{kT}{G\rho m_p}} \tag{1.7}$$

From this we can see that cool, dense gas clouds will collapse under their own gravity. Typically, the collapse of a star forming gas cloud begins isothermally. As densities rise, the free-fall time of the cloud decreases, and so in turn does the Jeans mass. This fuels fragmentation: small, dense clumps collapse faster than the parent cloud itself. Gas cooling through metal cooling lines or the formation of molecules (such as H_2) reduces the pressure

available to support a gas cloud against gravitational collapse. The opacity of the gas also increases with increasing density, and it is the rising opacity that finally halts fragmentation: with high enough opacity, the energy created through gravitational collapse cannot escape the cloud. The collapse then transitions from the isothermal regime to the adiabatic. Consequently, rising density yield rising temperature and pressure. Once the collapsing object reaches sufficient internal pressure to balance gravity, collapse ends. In the case of star formation in the local Universe, these collapsed objects are proto-stars.

In order to form a massive black hole in the early Universe, some process must take place to prevent fragmentation. What conditions would favor runaway collapse in place of fragmentation? Below a virial temperature of 10^4 K, the gas in a galaxy maintains densities lower than that of the dark matter, and so remains susceptible to tidal forces and is unlikely to condense without efficient cooling through the formation of molecular hydrogen (Begelman et al., 2006). For halos with $T_{vir} \gtrsim 10^4$ K, however, gas can collect at the center of the halo more easily (Bromm & Loeb, 2003). In the absence of H_2, only atomic-line cooling is available. The gas cannot cool much below this same temperature (~ 8000 K), and the gas collapse thereby continues to be nearly isothermal (Oh & Haiman, 2002). In addition to the required suppression of H_2, the gas must also efficiently release angular momentum during collapse to avoid fragmentation. Several angular momentum transport mechanisms such as the 'bars-within-bars' instability (Begelman et al., 2006) and gravitationally unstable disks (Lodato & Natarajan, 2006) have been suggested as possible sources of efficient angular momentum redistribution. While some fragmentation may occur if the Lyman-Werner radiation is not sufficiently high or the halo spin is not sufficiently low, such fragmented objects are still massive ($10^3 - 10^4\ M_\odot$) and may merge to form a central massive black hole seed (Suazo et al., 2019).

1.8 Cosmological simulations

The simulations that support this work were performed using the parallel N-body smoothed particle hydrodynamics simulation code Gasoline (Stadel, 2001; Wadsley et al., 2004, 2017). The simulation uses particles to represent dark matter, gas, and stars. Gravitational forces are calculated directly ($\mathcal{O}N^2$) for nearby particles, but gravitational forces for those particles at large separations are calculated according to a tree algorithm ($\mathcal{O}(N\log N)$). Gas quantities in these simulations are computed on a smoothed particle hydrodynamics framework using a density kernel of nearby particles.

In this work, we use cosmological zoom-in simulations to study the assembly of a single Milky Way-type galaxy by $z = 0$. To begin, we evolve a uniform dark matter-only box to $z = 0$. At the final redshift, we select a galaxy of interest. The particles that make up this galaxy are then re-simulated from the initial conditions at higher resolution, now considering the evolution of both dark matter and gas.

We generate initial conditions through the Zel'dovich approximation for the non-linear growth of large-scale structure (Zel'dovich, 1970). Cosmological N-body simulations like these begin at $z \sim 150 - 90$, well after the formation of the cosmic microwave background (CMB) at $z = 1100$. Beginning from an initial density spectrum representing the CMB, particle positions and velocities are evolved according to a displacement field to the starting redshift of the simulation. The two most widely known methods for generating cosmological initial conditions are the Zel'dovich approximation, which is accurate to first order, and second-order Lagrangian perturbation theory (2LPT) (Scoccimarro, 1998). While both of these techniques recreate accurate low-redshift halo mass functions, the Zel'dovich approximation suppresses the growth of rare density peaks, which is significant at high redshift. The difference between the first-order and second-order approximations is particularly pronounced at the onset of reionization: 2LPT produces more high-redshift sites suitable for population III star formation (and black hole formation) and doubles the volume of the reionized region of the Universe by $z = 6$ (Holley-Bockelmann et al., 2012).

In simulations such those used in this work, the goal is to study galaxies in their fully cosmological, dynamic environment. Consequently, the resolution of these simulation does not capture important physical processes that occur on length scales less than hundreds of parsecs, including star and black hole formation, black hole accretion and feedback, and gas physics. Instead, these physical processes are represented as sub-grid physical models.

1.9 Smoothed Particle Hydrodynamics

Smoothed particle hydrodynamics (SPH) is a numerical method for modeling fluid dynamics by discretizing a fluid into an ensemble of point-mass particles (Monaghan, 1992). SPH is Lagrangian: the coordinates follow the motion of the particles. This is an alternative to Eulerian fluid dynamics treatments such as mesh codes, which employ fixed spatial coordinates (see Agertz et al. (2007) for a comparison of particle and mesh-based techniques). The fundamental component of SPH is the smoothing kernel, W, which enables the computation of density from the distribution of these particles:

$$\rho_i = \sum_{j=1}^{N_{neighbors}} m_j W(h, r_{ij}), \tag{1.8}$$

where h is the variable smoothing length.

The smoothing kernel can take on the form of any monotonic function that weights contributions from particles nearer to the particle of interest higher than those from particles at larger distances. The simplest example of a smoothing kernel is the spherically-symmetric three-dimensional Gaussian function:

$$W(h, r_{ij}) = \left(\frac{1}{\pi h}\right)^{3/2} e^{-r_{ij}^2/h^2}. \tag{1.9}$$

One clear drawback from this type of smoothing kernel is the non-zero contributions to the density of particle i for neighbor particles with $r_{ij} >> h$. Alternatively, a spline kernel provides compact support to the smoothing kernel, so that contributions to the density of particle i from particles outside of the smoothing kernel are zero. A three-dimensional cubic spline, which is the framework for the SPH implementation in Gasoline, takes the form of (Monaghan, 1992):

$$W(h, r_{ij}) = \frac{1}{\pi h^3} \begin{cases} 1 - \frac{3}{2}(\frac{r_{ij}}{h})^2 + \frac{3}{4}\left(\frac{r_{ij}}{h}\right)^3 & \text{for } 0 < \frac{r_{ij}}{h} \leq 1 \\ \frac{1}{4}\left(2 - \frac{r_{ij}}{h}\right)^3 & \text{for } 1 < \frac{r_{ij}}{h} \leq 2 \\ 0 & \text{otherwise.} \end{cases} \tag{1.10}$$

Figure 1.3 shows a cartoon description of a spline smoothing kernel with compact support as it is applied to a distribution of particles. Only particles inside the radius of compact support contribute to the density calculation of particle i.

SPH provides numerous advantages, including conservation of energy, linear momentum, and angular momentum, the last of which is not guaranteed in alternative treatments of fluid dynamics. The use of particles also provides adaptive resolution for large dynamic range and density contrasts, as the resolution naturally follows mass. Despite these advantages, SPH does not naturally well represent instabilities that form at interfaces between fluid contact discontinuities.

Gasoline employs a modern SPH implementation that smooths over pressure in a geometric density mean in the SPH force expression (Ritchie & Thomas, 2001; Governato et al., 2015; Wadsley et al., 2017). This updated approach to SPH is optimized for the multi-phase gas of the interstellar medium and eliminates the artificial gas surface tension produced by classical SPH approaches. An important test of the performance of an SPH algorithm is the Kelvin-Helmholtz test: two fluids move past each other with different velocities, and an instability forms at the contact interface between the two fluids. The

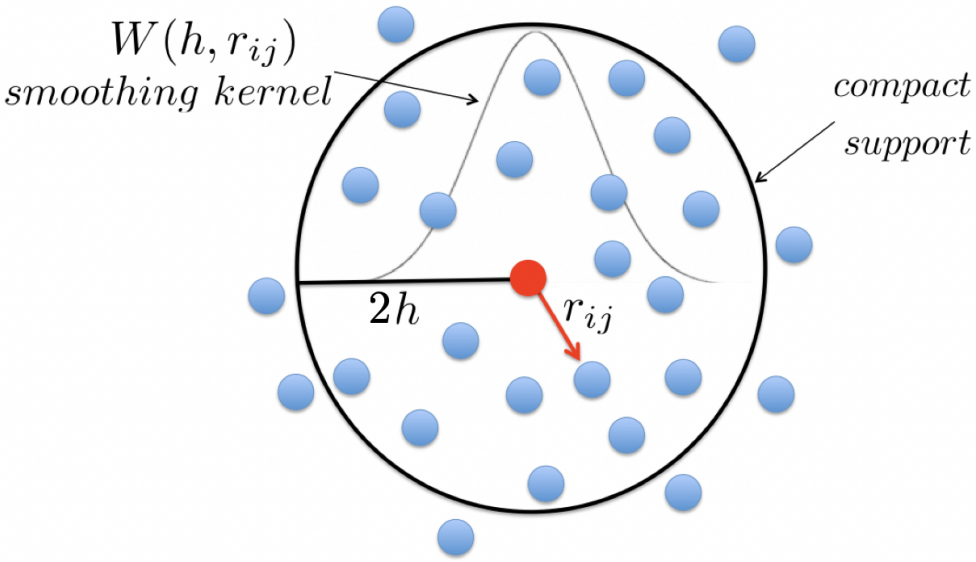

Figure 1.3: SMOOTHED PARTICLE HYDRODYNAMICS This figure depicts a cartoon example of a smoothed particle hydrodynamics spline smoothing kernel. The spline provides compact support to the smoothing kernel; all contributions for particles with $r > 2h$ are zero.

results of such a test comparing traditional SPH with modern SPH as implemented in Gasoline is shown in Figure 1.4. While traditional SPH prevents fluid mixing through artificial surface tension, modern SPH allows a Kelvin-Helmholtz instability to form.

1.10 Summary

In this Chapter, we presented some foundational information to support our discussion of the formation and assembly of massive black hole seeds in the first billion years of the Universe. In Chapter 2, we explore the theory direct collapse black hole *formation*, in which gas in pre-galactic halos can collapse monolithically into a massive black hole seed of $\sim 10^4 - 10^5\ M_\odot$. The goal of this work is to understand the most important physical processes that spawn massive black hole seeds in dark matter halos without presuming global halo properties required for formation. This is the first such study to constrain the demographics of direct collapse SMBHs and their hosts within a cosmological volume. In Chapter 3, we explore the *assembly* of massive black hole seeds through black hole-black hole mergers. Here we investigate the possibility that lower-redshift electro-magnetic or gravitational wave observables of massive black holes could contain imprints of the mass assembly history of the original seed black holes. In Chapter 4 we provide a general overview of this work and look forward towards future work in this field of study.

Over the next two decades, observational astronomy will likely yield a number of pivotal breakthroughs that will revolutionize the study of massive black hole seeds. The opacity of the Universe prior to re-ionization completely obscures the physical processes that create supermassive black holes before the Universe is even a tenth of its current age. Presently, observations of supermassive black holes are limited to the quasar epoch or lower redshifts, at which time the supermassive black hole has already accumulated $10^6 - 10^9 M_\odot$ of mass.

As we enter the epoch of gravitational wave astronomy, with the first observations of

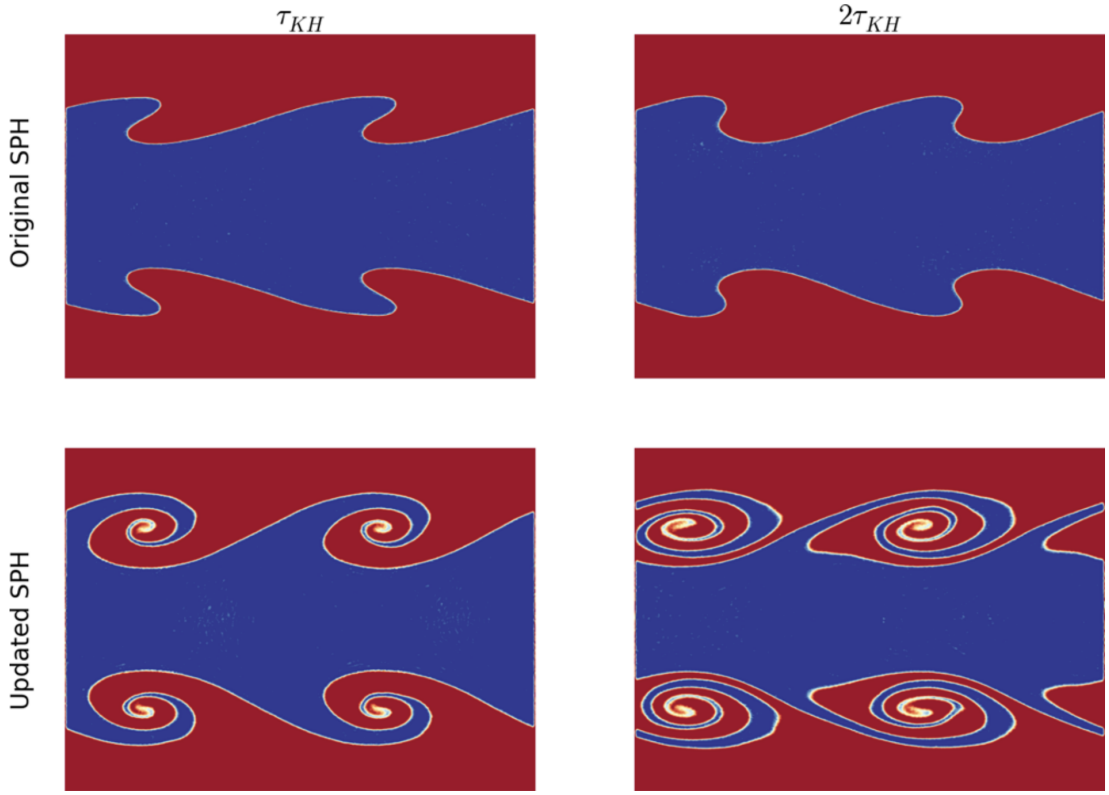

Figure 1.4: KELVIN-HELMHOLTZ INSTABILITY TEST FOR SPH This figure, selected from Governato et al. (2015), demonstrates the improved performance of the modern SPH (bottom panel) implementation in a Kelvin-Helmholtz instability test as compared to traditional SPH (top panel). In the original SPH formalism, artificial surface tension can suppress the formation of a Kelvin-Helmholtz instability, preventing the mixing of multi-phase gas. The geometric density mean, in combination with turbulent diffusion (Shen et al., 2010), allows the instability to form.

merging binary black holes with the Laser Interferometer Gravitational-Wave Observatory (LIGO) (Abbott et al., 2016), we may soon peer into the cosmological dark ages for the first time. The upcoming Laser Interferometer Space Antenna (*LISA*) promises to provide some of the first observational clues about the formation of massive black hole seeds. *LISA* science objectives include the goal to trace the origin and assembly of massive black holes across cosmic time. This translates into specific science investigations including the detection of inspiraling binary black holes in a mass range of $\sim 10^3 - 10^5 M_\odot$ at a redshift range of $10 - 15$ and coalescing binary black holes in a mass range of $\sim 10^4 - 10^6 M_\odot$ at redshifts less than 9 (Amaro-Seoane et al., 2017). Such detections will provide some of the first observational constraints on the origins and early growth of supermassive black holes.

Chapter 2

Sowing black hole seeds: Direct collapse black hole formation with realistic Lyman-Werner radiation in cosmological simulations

This chapter was previously published in collaboration with Jillian Bellovary, Kelly Holley-Bockelmann, Charlotte Christensen, and Tom Quinn in the July 2018 edition of The Astrophysical Journal (Dunn et al., 2018). It appears here with minor formatting changes.

In this chapter, we study the birth of supermassive black holes from the direct collapse process and characterize the sites where these black hole seeds form. In the pre-reionization epoch, molecular hydrogen (H_2) is an efficient coolant, causing gas to fragment and form Population III stars, but Lyman-Werner radiation can suppress H_2 formation and allow gas to collapse directly into a massive black hole. The critical flux required to inhibit H_2 formation, $J_{\rm crit}$, is hotly debated, largely due to the uncertainties in the source radiation spectrum, H_2 self-shielding, and collisional dissociation rates. Here, we test the power of the direct collapse model in a self-consistent, time-dependant, non-uniform Lyman-Werner radiation field – the first time such has been done in a cosmological volume – using an updated version of the SPH+N-body tree code GASOLINE with H_2 non-equilibrium abundance tracking, H_2 cooling, and a modern SPH implementation. We vary $J_{\rm crit}$ from 30 to 10^3 in units of J_{21} to study how this parameter impacts the number of seed black holes and the type of galaxies which host them. We focus on black hole formation as a function of environment, halo mass, metallicity, and proximity of the Lyman-Werner source. Massive black hole seeds form more abundantly with lower $J_{\rm crit}$ thresholds, but regardless of $J_{\rm crit}$, these seeds typically form in halos that have recently begun star formation. Our results do not confirm the proposed atomic cooling halo pair scenario; rather black hole seeds predominantly form in low-metallicity pockets of halos which already host star formation.

2.1 Introduction

The detections of luminous quasars at redshifts $z \gtrsim 6$ (e.g., Fan et al., 2003; Kurk et al., 2007; Mortlock et al., 2011; De Rosa et al., 2014; Bañados et al., 2016) indicate that the first black holes formed early and grew to $10^6 - 10^9 M_\odot$ within the first billion years after the Big Bang. While the formation mechanism and early growth of these massive black holes (MBH) is widely debated, these objects likely formed from massive 'seed' black holes (Haiman & Loeb, 2001) within the first few hundred million years after the Big Bang and accumulated mass swiftly to produce the observable distribution of high-redshift quasars (Volonteri et al., 2003). The evolution of an MBH and its host halo are integrally tied, and this relationship can be harnesses to explore heirarchical structure formation (e.g., Micic et al., 2007) and probe MBH demographics (e.g., Micic et al., 2008; Volonteri & Natarajan, 2009).

One popular model of MBH formation proposes that MBH seeds with masses of $100 M_\odot$ form from the remnants of high-mass population III stars (Madau & Rees, 2001; Heger & Woosley, 2002; Johnson & Bromm, 2007)(see, however, Stacy et al. (2010); Hosokawa et al. (2011)). Such low-mass seeds may serve as building blocks for supermassive black holes through both MBH-MBH mergers and gas accretion (e.g., Micic et al., 2007; Holley-Bockelmann et al., 2010). A second possible formation channel may be through stellar collisions in a dense nuclear star cluster (Begelman & Rees, 1978; Devecchi & Volonteri, 2009; Davies et al., 2011; Katz et al., 2015; Yajima & Khochfar, 2016). A third theory, which we study in this paper, is that MBHs form by the direct isothermal collapse of pristine gas within a primordial dark matter halo (Loeb & Rasio, 1994; Haiman et al., 1996; Koushiappas et al., 2004; Begelman et al., 2006; Lodato & Natarajan, 2006; Haiman, 2006; Spaans & Silk, 2006; Shang et al., 2010; Prieto et al., 2013; Latif et al., 2013a,c; Johnson et al., 2014;

Choi et al., 2015; Glover, 2016; Yue et al., 2017). Because the seeds are massive in this model, direct collapse has been invoked to explain the massive quasars at high redshift (Natarajan et al., 2017). In this work, we study the demographics of direct collapse black hole formation sites in the context of fully cosmological simulations with a self-consistent radiation field.

In this paper, we consider thermodynamic direct collapse enabled by Lyman-Werner radiation. Alternative mechanisms that may suppress fragmentation could allow early dark matter halos to remain dynamically hot and support the gas against collapse despite efficient thermal cooling. Baryonic streaming velocities, left over from baryon-photon fluid decoupling at recombination, increase the random motion of gas in high-redshift halos and may delay collapse long enough to allow these halos to acquire enough mass to enable preferential formation of MBH seeds (Schauer et al., 2017b; Tanaka & Li, 2014; Hirano et al., 2017). Dynamical heating effects due to the rapid growth of halos through accretion and mergers can also foster random motion of gas in high-redshift halos and may delay collapse, effectively increasing the final mass of the collapsing object (Yoshida et al., 2003).

Conditions that would permit thermodynamic direct collapse to proceed without fragmentation are likely rare, as it requires that the Jeans mass of the collapsing cloud remain large. This environment is expected to only occur in pristine atomic cooling halos with $T_{vir} > 10^4$K, corresponding to a redshift dependent minimum halo mass of $M_{halo} > 3 \times 10^7 M_\odot [(1+z)/11]^{-3/2}$ (Visbal et al., 2017; Barkana & Loeb, 2001). Furthermore, these halos must have metallicity $\mathrm{Z/Z_\odot} \leq 5 \times 10^{-6} - 10^{-5}$ (Omukai et al., 2008; Clark et al., 2008; Latif et al., 2016) and experience intense Lyman-Werner radiation from a nearby starforming region (Latif et al., 2013c; Regan et al., 2014). These constraints imply a small window of opportunity for MBH formation in cosmic time, halo mass, and location.

If gas cools too quickly, it easily fragments; in essence, the direct collapse model relies on removing efficient gas cooling channels. Before the first stars enriched their host halos with metals, the primary coolant for halos below a virial temperature of $\sim 8,000$K is molecular

Hydrogen (H_2). In this scenario, the gas must remain pristine not only because metal-line cooling enhances fragmentation, but because Hydrogen molecules H_2 and HD form readily on dust grains (Cazaux & Spaans, 2009), adding another avenue for cooling to proceed efficiently. Without H_2 or metals, gas in these proto-galactic halos can only cool though collisional excitation of atomic Hydrogen. Atomic hydrogen cannot cool the gas below T$\sim 10^4$ K, resulting in a Jeans mass of $10^4 - 10^5 M_\odot$. To clear a halo of H_2, its gas must be irradiated with UV photons to photo-dissociate any molecular Hydrogen within; naturally the energy range to disrupt H_2 corresponds to the Lyman and Werner absorption bands between 11.2 - 13.6 eV. This specific intensity necessary to suppress molecular Hydrogen in atomic cooling halos is known as $J_{\rm crit}$, and is expressed in units of J_{21} (10^{-21} erg s^{-1} cm^{-2} sr^{-1} Hz^{-1}).

In summary, a halo with a virial temperature $T_{\rm vir} \geq 10^4 K$ exposed to Lyman-Werner radiation in excess of a critical threshold, $J_{\rm crit}$, can collapse isothermally under its own gravity directly into a black hole, without fragmenting to form stars (Shang et al., 2010; Latif et al., 2014). The critical value of Lyman-Werner radiation required to prevent H_2 formation in a halo, $J_{\rm crit}$, is unknown, and possible values presently span several orders of magnitude, reaching as low as 30 if produced by a soft stellar spectrum or as high as 10^4 from a hard stellar spectrum (Shang et al., 2010; Glover, 2015b). Complicating the simple picture of a single radiation threshold, Sugimura et al. (2014), Agarwal et al. (2016) and Wolcott-Green et al. (2017) argue that in fact there may be no universal $J_{\rm crit}$, but instead that the gas density, as well as the mass, age and distance to the Lyman-Werner source all generate variable Lyman-Werner irradiation that ultimately manifests in halo-to-halo variations in $J_{\rm crit}$.

Following the lead of theoretical and semi-analytic studies (Dijkstra et al., 2008; Ahn et al., 2009; Dijkstra et al., 2014), the bulk of numerical work has focused on treatments in which seed MBHs form according to prescribed global halo properties. Agarwal et al. (2014) restricted their studies of direct collapse formation sites to halos that are strictly metal

free, with no star formation history, and have only been exposed to Lyman-Werner radiation from non-local sources. Habouzit et al. (2016) used several different volume cosmological simulations to identify direct collapse seed locations in metal-poor atomic cooling halos testing three different $J_{\rm crit}$ values and two different formation timescales. Tremmel et al. (2017) used state-of-the-art cosmological simulations constructed with ChaNGa to model MBH seed formation in metal-poor, rapidly collapsing, slowly cooling gas particles, but does not consider the role of Lyman-Werner radiation or H_2 cooling. The black holes in these simulation grow nearly instantaneously to 10^6 $M_\odot$. Several of the modern interpretations of the direct collapse model invoke the synchronization of two neighboring atomic cooling halos separated by less than 1-2 kpc. One halo experiences a burst of star formation that provides enough Lyman-Werner radiation to prevent star formation in the neighboring halo (see e.g., Dijkstra et al., 2008; Shang et al., 2010; Visbal et al., 2014a; Regan et al., 2014, 2017; Wolcott-Green et al., 2017).

In this work, we study the formation of direct collapse MBH seeds as governed by a self-consistently modeled, non-uniform Lyman-Werner radiation field in a cosmological volume. This seeding method makes no assumptions about the global properties of the halos that form MBHs, nor does it make any requirements of the halo's history. Instead, MBH seeds form from gas particles according to the local gas properties and Lyman-Werner radiation levels. This allows us the unique opportunity to study the direct collapse model in a fully self-consistent environment and extract halo properties of MBH hosts in post-processing. This work is the first ever treatment of massive black hole formation based solely upon local gas physics in a cosmological context to include a self-consistent spatially and temporally varying Lyman-Werner radiation field.

The paper is organized as follows: in Section 3.2 we discuss the simulation suite; in Section 2.3.1 we discuss the role of Lyman-Werner radiation in direct collapse; in Section 2.3 we outline our MBH seed formation algorithm; and in Section 3.4 we discuss the implications of low-$J_{\rm crit}$ MBH formation models for low-redshift MBH distributions.

2.2 Simulations

In this work, we use the N-body+Smooth Particle Hydrodynamics (SPH) tree code GASOLINE (Stadel, 2001; Wadsley et al., 2004, 2017) to study the formation of MBH seeds in cosmological simulations. GASOLINE has previously been shown to form galaxies that follow the Tully-Fisher relation (Governato et al., 2009), the halo mass-metallicity relationship (Brooks et al., 2007), the stellar mass − halo mass relation (Munshi et al., 2013), size-luminosity relation (Brooks et al., 2011), and produce realistic disks, bulges, and star formation histories (Christensen et al., 2010, 2014).

This implementation of GASOLINE includes a geometric density average in the SPH force expression (Ritchie & Thomas, 2001). The treatment of gas physics includes an H_2 non-equilibrium abundance tracking and cooling procedure, a sophisticated treatment of H_2 abundance calculations that account for self-shielding, collisional dissociation, and dust grain formation and shielding (Christensen et al., 2012). We also consider the photo-dissociation rate due to spatially and temporally varying Lyman-Werner flux produced self-consistently by stars in the simulation, (Christensen et al., 2012) (see Section 2.3.2 for a more complete discussion of the implementation and role of Lyman-Werner radiation in these simulations). In addition to H_2 cooling, the simulation includes metal-line cooling and turbulent metal diffusion (Shen et al., 2010). The simulation includes a uniform background ionizing radiation beginning at a redshift of $z = 9$ (Haardt & Madau, 1996), which is independent of the Lyman-Werner radiation generated by stars. The simulation also includes the Sedov solution blast-wave supernova feedback energy with a blast-wave energy of $E_{SN} = 8 \times 10^{50}$ erg (Stinson et al., 2006). Star formation occurs stochastically according to a Kroupa stellar initial mass function (Kroupa, 2001), with a probability that depends on the H_2 fraction of the gas. GASOLINE also includes physically motivated prescriptions

for black hole formation, accretion, feedback and mergers (Bellovary et al., 2010). For the first time, we include a revised black hole formation prescription featuring a probabilistic function that depends on the local Lyman-Werner flux, J_{LW}. We discuss the implementation of star formation and MBH seed formation physics in GASOLINE and our modifications to the black hole formation model are discussed in Section 2.3.

We tested three different values of $J_{\rm crit}$, spanning the range of predicted values ($J_{\rm crit} = 10^3 J_{21}$ $300 J_{21}$, and $30 J_{21}$, see Section 2.3) by examining black hole formation in a Milky Way-analog disk galaxy ($h258$). The evolution of this halo has previously been studied in detail (see e.g., Bellovary et al., 2010, 2011; Zolotov et al., 2012; Munshi et al., 2014; Christensen et al., 2016). The initial conditions for this galaxy were selected from a 50 Mpc uniform dark matter-only simulation that was re-simulated at a higher resolution via volume renormalization (Katz & White, 1993). At $z = 5$, the main progenitor of this halo has reached a mass of $8.5 \times 10^9 M_\odot$. Each of the simulations has a dark matter mass resolution of $3.7 \times 10^4 M_\odot$, a gas mass resolution of $2.7 \times 10^4 M_\odot$, a stellar mass resolution of $8 \times 10^3 M_\odot$ and a spline kernel softening length of 0.173 kpc. Since the focus of this work is the era of MBH formation, we evolve our simulations from the initial redshift of $z = 149$ to $z = 5$.

The simulations are fully cosmological, initialized at $z = 149$ with the Zel'dovich approximation and WMAP3 cosmology: $\Omega_m = 0.24$, $\Omega_b = 0.042$, $\Omega_\Lambda = 0.76$, $h = 0.73$, $\sigma_8 = 0.77$, and $n = 0.96$ (Spergel et al., 2007). We note here that previous work has shown that halos in cosmological simulations initialized with the Zel'dovich approximation form later, leading to later black hole formation, than in simulations initialized with second-order Lagrangian perturbation theory (Holley-Bockelmann et al., 2012). We identified halos using the Amiga Halo Finder (Gill et al., 2004; Knollmann & Knebe, 2009), which employs isodensity surfaces to identify gravitationally bound objects, to identify halos with more than 64 particles. Halo centers are identified using the shrinking-sphere method of Power et al. (2003) as implemented in Pynbody (Pontzen et al., 2013). We consider halos with more than 10^3 particles, corresponding to a minimum mass of $\sim 10^7 M_\odot$, well resolved. We note here

that this resolution allows us to resolve most atomic cooling halos, which would have a minimum mass of $\sim 2-3\times10^7 M_\odot$ during the period of peak MBH formation. In Figures 2.1 and 2.2, we show a line-of-sight averaged image of the gas, colored by density, in the high-resolution region of the $J_{crit} = 10^3 J_{21}$ simulation at $z = 5$. The locations of MBH seeds are marked by open black circles. At the end of the simulation, there are 15 MBHs in the $J1000$ simulation, three of which reside in the most massive halo. Several halos host more that one MBH by $z = 5$.

2.3 MBH seed formation and evolution

2.3.1 Lyman-Werner radiation and the atomic cooling regime

The current range of possible $J_{\rm crit}$ values spans several orders of magnitude (Haiman et al., 2000; Latif et al., 2013b; Aykutalp et al., 2014; Latif et al., 2015). The uncertainty in this value stems in part from the spectral shape of the radiation sources providing the Lyman-Werner radiation (Latif et al., 2014), the H_2 self-shielding model (Wolcott-Green et al., 2011), and the gas chemistry model (Glover, 2015a). Beyond these model-dependent uncertainties, it is possible that there is no universal $J_{\rm crit}$ value (Agarwal et al., 2016) but instead that there is critical relationship between the rate of photo-dissociation of H_2 molecules by Lyman-Werner photons and the rate of photo-detachment of H^- by infrared light that governs whether the H_2 fraction rises high enough to enable catastrophic cooling and fragmentation (Wolcott-Green et al., 2017). Even so, it is clear that some minimum level of Lyman-Werner radiation is necessary to fully suppress molecular Hydrogen cooling; if the incident flux is lower than $\sim 10 J_{21}$, fragmentation is not prevented but only delayed, and may ultimately yield increased fragmentation (Regan & Downes, 2018).

The direct collapse model of MBH seed formation requires that $10^4 - 10^6 M_\odot$ of gas loses enough angular momentum to rapidly collapse, with gas inflow rates $\geq 0.1 M_\odot/\mathrm{yr}$ for

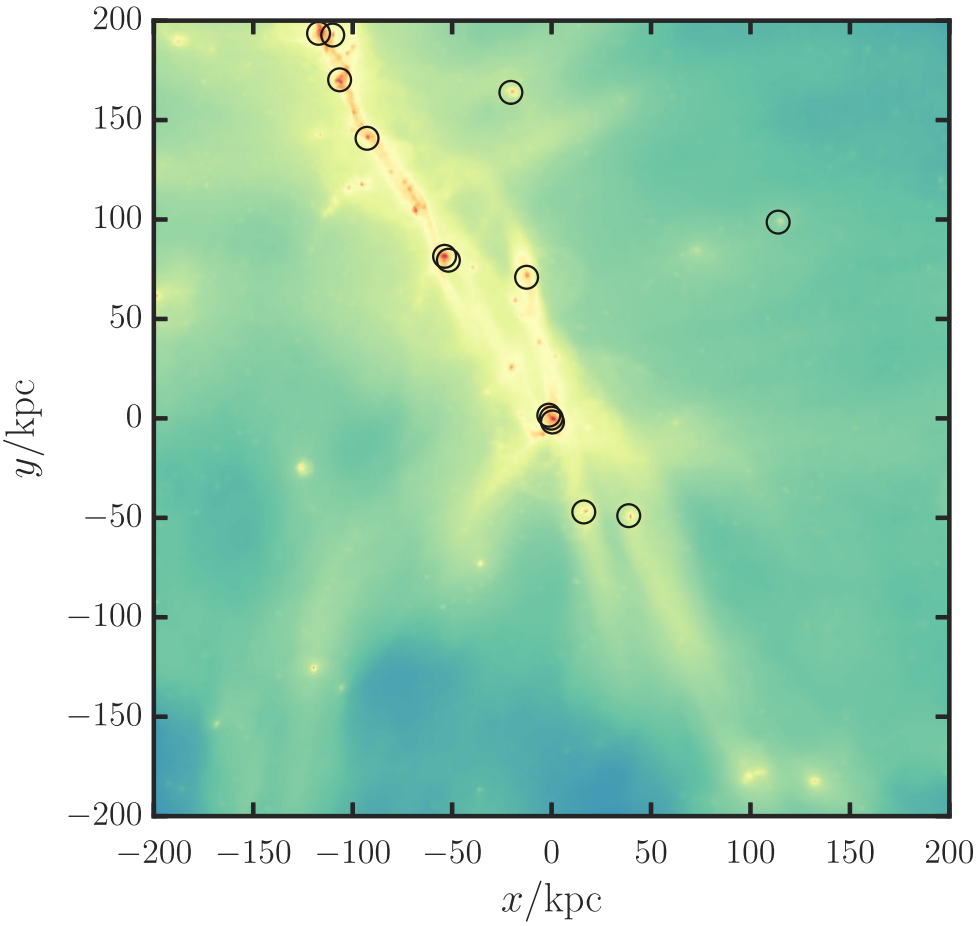

Figure 2.1: MBH FORMATION SITES AT REDSHIFT 5Massive black hole seed positions are marked by black circles in this $z = 5$ gas surface density image of the $h258$ progenitor halos constructed from the $J1000$ simulation. The image is centered on the most massive progenitor halo at this redshift, which hosts three MBH seeds.

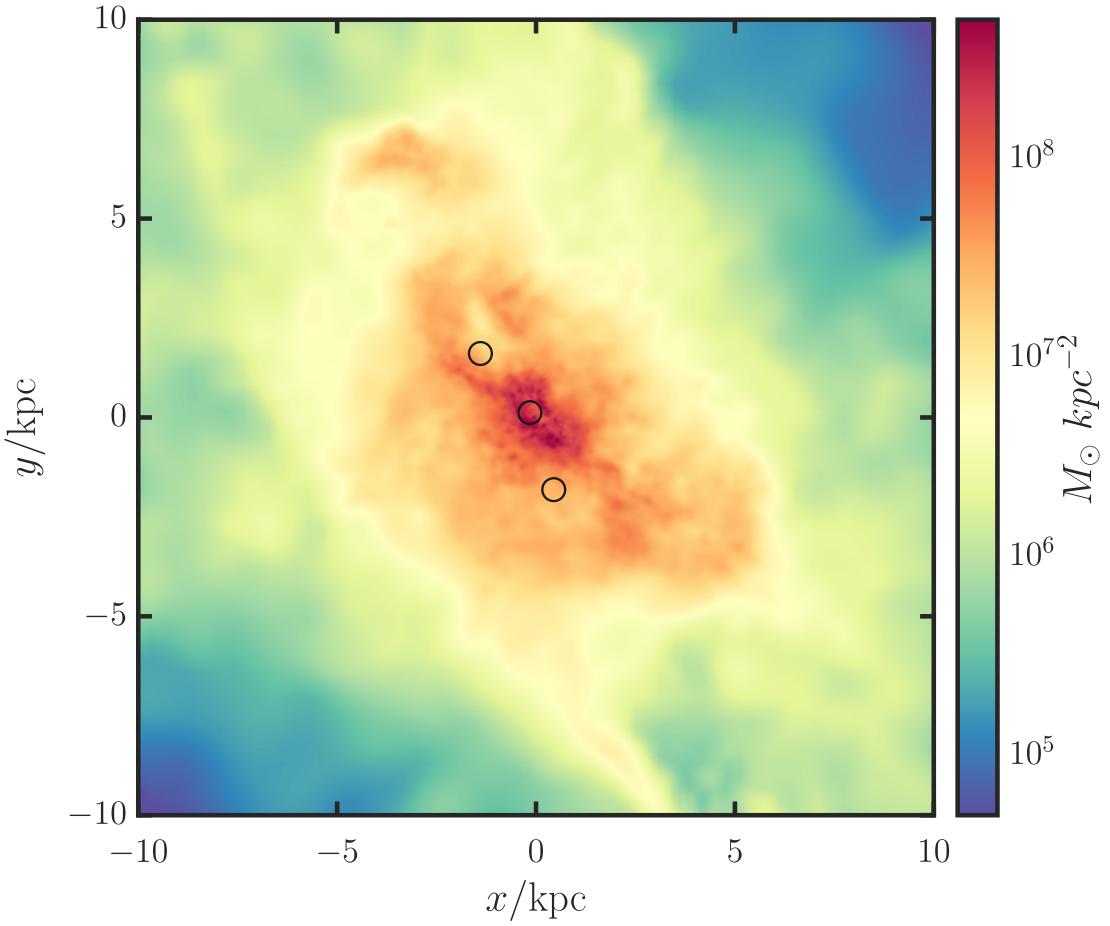

Figure 2.2: MBH FORMATION SITES AT REDSHIFT 5 An enlarged image of the most massive progenitor halo at $z = 5$ shows that this $2.7 \times 10^{10} M_\odot$ protogalaxy hosts three centrally located MBHs, the most massive of which is $2.7 \times 10^5 M_\odot$.

$\sim 1 - 10$ Myr (Hosokawa et al., 2013; Alexander & Natarajan, 2014; Umeda et al., 2016). The dissipation of large amounts of angular momentum has been a major theoretical hurdle for the direct collapse model, and has been the subject of much work. While some authors have restricted the direct collapse domain to only low angular momentum halos (Eisenstein & Loeb, 1995) or material in the low-angular momentum tail of the specific angular momentum distribution in dark matter halos (Koushiappas et al., 2004), other authors have explored mechanisms of angular momentum transport. Work by Dubois et al. (2012b) has shown that a significant fraction of the gas entering a high-z halo can stream directly to the central bulge through efficient angular momentum re-distribution. Such large accretion rates allow the gas to collapse without fragmenting to form stars and can occur through dynamical processes, such as the 'bars-within-bars' gravitational instability (Shlosman et al., 1989; Begelman et al., 2006; Lodato & Natarajan, 2006), torques, and turbulence (Choi et al., 2013, 2015). Furthermore, these angular momentum transport mechanisms can actually serve to further suppress gas fragmentation (Begelman & Shlosman, 2009; Choi et al., 2015).

Work by Lodato & Natarajan (2006, 2007) has shown that low-angular momentum halos can provide favorable conditions for direct collapse; low-mass halos with large spin are less likely to form direct collapse black holes. While some authors choose to require direct collapse occur only in low-spin halos (e.g., Volonteri, 2010; Agarwal et al., 2013), we do not apply such a criterion because it is not consistent with our recipe for MBH formation based solely of local gas physics. Furthermore, the available angular momentum transport processes would occur below our resolution limit (Choi et al., 2013). Such a requirement has previously been excluded in other work (e.g., Bonoli et al., 2014) based on the justification that the dark matter and gas angular momentum are decoupled at scales below the virial radius.

2.3.2 Implementing the direct collapse model in GASOLINE

MBH seed formation in GASOLINE is designed to emulate the existing star formation physics in the code. The star formation module allows cold, dense gas particles undergoing local gravitational collapse ($\nabla \cdot v < 0$) to form stars stochastically, following a probabilistic function that depends on the molecular hydrogen abundance and the dynamical formation time of the particle (Christensen et al., 2012). The gas density must exceed the threshold density for star formation of 0.1 cm^{-3} and must be colder than 10^4 K, however, work by (Christensen et al., 2012) demonstrated that a star formation recipe driven by the H_2 fraction of the gas provides a more realistic spatial distribution of star formation in spiral galaxies. The dependence of the star formation efficiency on the H_2 fraction supersedes the density and temperature thresholds by preferentially forming stars in regions abundant in molecular Hydrogen. If a gas particle meets all of the relevant criteria, the probability that it will form a star is given by

$$P = \frac{m_{gas}}{m_{star}} \left(1 - e^{c^* X_{\mathrm{H}_2} \Delta t / t_{form}}\right) \tag{2.1}$$

in which the prefactor is the ratio of gas particle to initial star particle mass, c^* is a free parameter set to 0.1 to recreate observable relations including the Kennicut-Schmidt law and Tully-Fischer law (Governato et al., 2010), t_{form} is the dynamical time for the gas particle, and Δt is the interval between star formation episodes, set to 1 Myr.

Similarly, we allow MBH seeds to form stochastically from gas particles in environments that meet the convergence and temperature requirements for star formation. Gas particles considered for black hole candidacy must be 100 times more dense than star forming gas (10 cm^{-3}), metal free to a tolerance of $Z < 10^{-6}$, and experience Lyman-Werner radiation above a tuneable threshold that we specify at runtime, J_{crit}. If a gas particle meets the minimum MBH formation criteria, it is assigned a formation probability modeled after that used for star formation:

$$P_{BH} = 1 - e^{\frac{-J}{J_{\mathrm{crit}}} \Delta t / t_{form}} \tag{2.2}$$

in which J is the local Lyman-Werner flux level and $J_{\rm crit}$ is the critical Lyman-Werner radiation threshold employed in the simulation.

The Lyman-Werner radiation from stars in GASOLINE is modeled as a function of stellar mass and age, as described in detail in Christensen et al. (2012). The Lyman-Werner stellar luminosity is calculated as a function of the age and mass of the star particle via STARBURST99 (Leitherer et al., 1999) synthesis models for starforming regions assuming a Kroupa et al. (1993) initial mass function. The Lyman-Werner flux then propagates using the gravitational tree structure to approximate locality and assuming optically thin gas. Christensen et al. (2012) tested the accuracy of the Lyman-Werner model with a set of isolated disk galaxies from which they found that the computed Lyman-Werner flux value is within a factor of ten of the theoretical Lyman-Werner flux value in the optically thin limit.

The GASOLINE black hole formation module allows MBH seeds to form without regard to global halo properties or the gas particle's position in the halo; rather, only the local gas properties dictate MBH seed formation. This approach has the strong advantage that MBHs are not required to "know" anything about the large-scale properties of its parent halo. MBH seeds are represented by sink particles, and form at a mass of $2.7 \times 10^4 M_{\odot}$, taking on the entire mass of the parent gas particle.

Black holes in GASOLINE are allowed to grow via isotropic gas accretion according to the Bondi-Hoyle formalism (Bellovary et al., 2010). Gas accretion is capped at the Eddington limit, assuming 10% radiative efficiency. A fraction of the rest-mass energy of the accreted gas is converted to thermal energy, which is then isotropically distributed to the surrounding gas (Di Matteo et al., 2005). This energy dissipates according to a blast-wave feedback approach similar to the supernova feedback recipe of Stinson et al. (2006), in that each affected particle's cooling is disabled for the duration of that particle's accretion time step. MBH seeds can also grow through MBH-MBH mergers, which occur when the separation between two sink particles is less than two softening lengths and their relative velocities are small: $\frac{1}{2}\Delta\vec{v}^2 < \Delta\vec{a}\cdot\Delta\vec{r}$, where $\Delta\vec{v}$ and $\Delta\vec{a}$ are the differences in velocity and

Name	$J_{\rm crit}$	N_{seed}	N_{BH} at $z=5$	$\max(M_{BH}/M_{\odot})$ at $z=5$	z_{first}	z_{last}
$J1000$	$10^3 J_{21}$	67	15	2.7×10^5	28	9.7
$J300$	$300 J_{21}$	124	24	5.9×10^5	28	8.7
$J30$	$30 J_{21}$	849	88	3.1×10^6	24	5

Table 2.1: SIMULATION PARAMETERS Summary of selected results of the simulations presented in this paper. (1) Simulation name, (2) $J_{\rm crit}$ in units of J_{21} (10^{-21} erg s^{-1} cm^{-2} sr^{-1} Hz^{-1}), (3) Total number of MBH seeds formed, (4) Number of black holes at $z=5$, (5) Mass of the most massive black hole at $z=5$, (6) Redshift of the first MBH seed formation event, (7) Redshift of the final MBH seed formation event.

acceleration of the two black holes, and $\Delta\vec{r}$ is their separation.

While our MBH seed model does not proscribe multiplicity of MBH seeds in a single halo, we include a mechanism to prevent spurious MBH overproduction. We allow multiple MBH seeds to form at the same time step only if the particles are separated by more than the black hole merger separation criterion of two softening lengths. If more than one gas particle meets the MBH formation criteria within this volume, only the most bound particle becomes an MBH seed, and the remaining MBH candidates revert to their parent gas particles. Since black hole accretion and feedback occur on the smallest timescales in the simulation, this code modification gives the MBHs an opportunity to modify their environments via accretion feedback before the next episode of star and black hole formation, thus preventing the formation of multiple black hole particles in one place at effectively the same time.

2.4 Results

2.4.1 Massive black hole seed formation

Table 3.1 summarizes our simulations and characterizes the number, maximum mass, and formation epoch of MBH seeds. Note the vast difference between the $J30$ results and

the higher Lyman-Werner thresholds. A lower $J_{\rm crit}$ allows more MBH seeds to form, allows seeds to form at lower redshifts, and increases the final mass of the most massive MBH by redshift 5. While this trend holds true in all runs, the difference between the $J300$ and $J30$ simulations is extreme.

Figure 2.3 takes a census of MBHs in each experiment. Regardless of $J_{\rm crit}$, MBH seeds begin to form within the first 0.2 Gyr. Solid lines show the number of MBHs present in each simulation, whereas the dashed lines show the total number of MBH seeds that have ever formed in each simulation. By comparing the solid and dashed lines, we can see a rapid series of MBH mergers between z$\sim 15-10$. This active merger epoch takes place before reionization, making it unlikely to observe using electromagnetic messengers but a promising source of gravitational waves detectable by LISA (Amaro-Seoane et al., 2017). MBH formation diminishes rapidly after $z\sim 9$ in all simulations, but decreasing $J_{\rm crit}$ prolongs the epoch of seed formation.

Figure 2.4 compares the redshift evolution of black hole formation and star formation in the three simulations. Though the number of MBH seeds differs, all three runs feature a peak in MBH seed formation near $z=12-10$ and rapidly drops off thereafter. Though the $J30$ simulation continues to make a few new MBH seeds at lower redshifts, by $z=5$ most halos are sufficiently polluted with metals to quench MBH seed formation (Bellovary et al., 2011). Still, we observe some seeds still forming at the end of our simulations, hinting at the possibility of a rare population of MBH seeds forming at low redshit.

The occupation fraction of massive black holes, particularly in local dwarf galaxies (Miller et al., 2015), likely encodes information about the MBH formation process. This metric may provide clues as to the initial MBH seed mass (van Wassenhove et al., 2010), the MBH formation efficiency (Volonteri et al., 2008), merger history (Menou et al., 2001), and the relative contribution of early and late MBH formation epochs (Tanaka & Haiman, 2009). Unfortunately, the high redshift occupation fraction is highly uncertain (Lippai et al., 2009). We define the MBH occupation fraction as the fraction of halos in a mass bin of

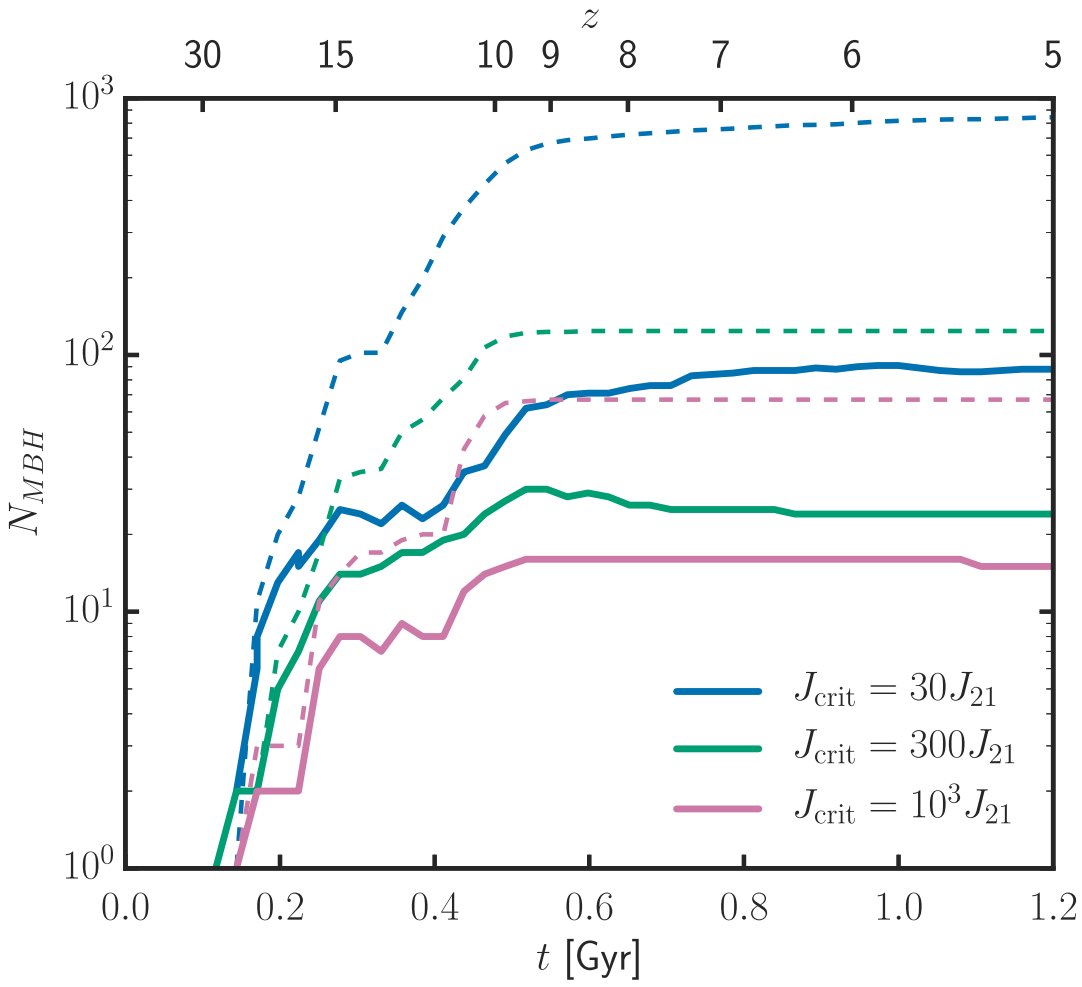

Figure 2.3: CENSUS OF MBH FORMATION Solid lines show the number of MBHs present in each simulation over time. The dashed lines show the total number of MBH seeds that have ever formed in each simulation. MBH-MBH mergers account for the discrepancies between the total number of MBH seeds that have ever formed by a specific redshift and the current number of MBHs at that time.

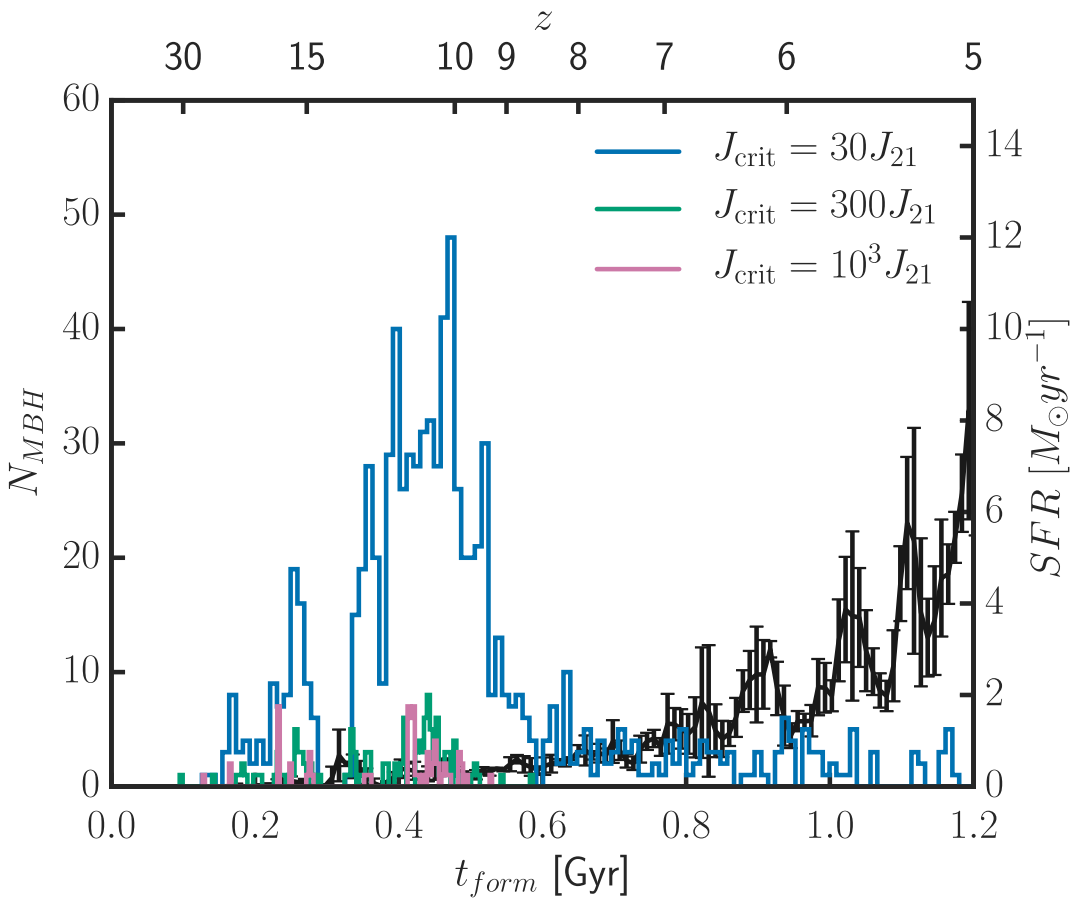

Figure 2.4: MBH FORMATION RATES The mean star formation history of the three simulations is shown in black with one-sigma error bars to demonstrate the variation in star formation rate between the three simulations. The MBH formation rate of the three simulations shows that lower $J_{\rm crit}$ values allow not only more MBH seeds to form, but additionally that a low $J_{\rm crit}$ threshold allows MBH seeds to form after MBH formation has dropped off with larger $J_{\rm crit}$ thresholds. At high redshift, $z \gtrsim 15$, MBH formation occurs in sporadic bursts. The rate of MBH formation peaks in all three simulations before $z = 10$. Only in the $J30$ simulation, with the most lenient MBH formation criteria, do MBH seeds form later than $z = 9$, and may continue after $z = 5$.

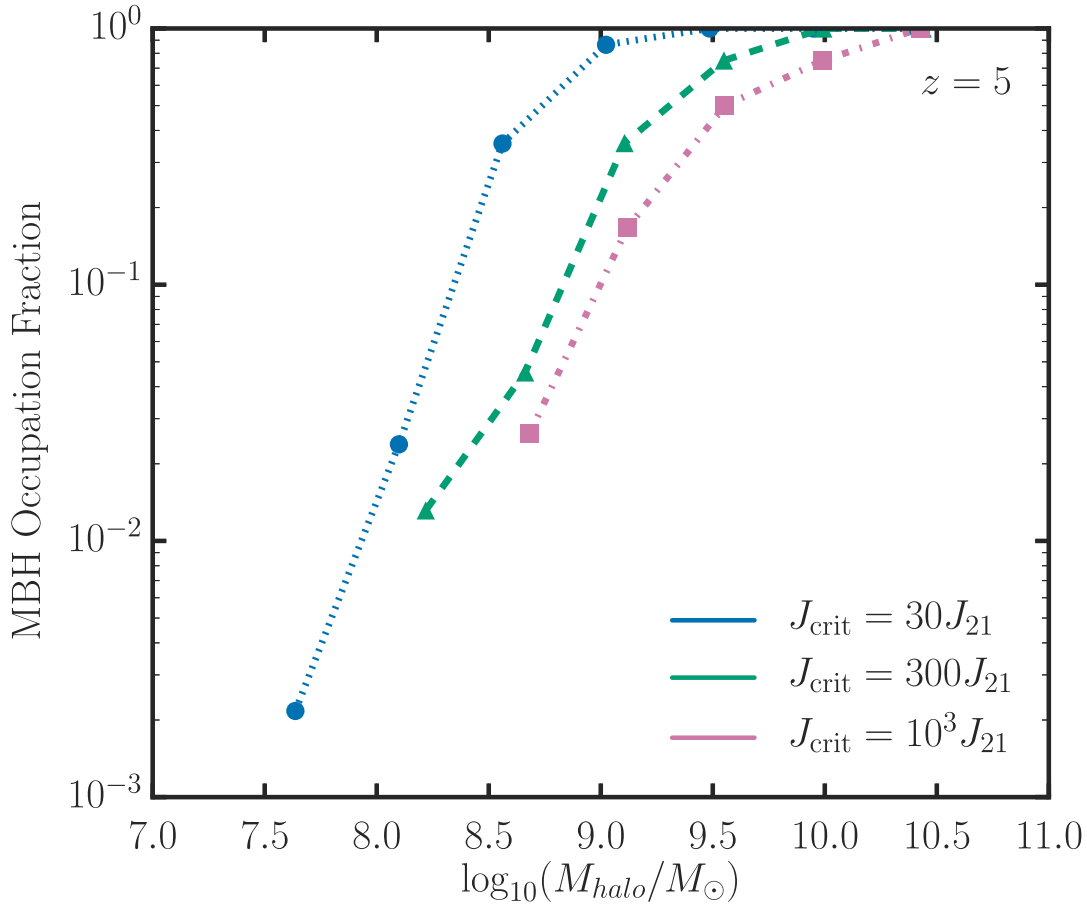

Figure 2.5: MBH OCCUPATION FRACTIONS A comparison of the MBH halo occupation fractions from simulations with three different $J_{\rm crit}$ values shows that lower $J_{\rm crit}$ thresholds allow MBH seeds to form in lower-mass halos, and that low-mass halos are more likely to host MBHs. At $z = 5$, a minimum of half of all halos more massive than $3 \times 10^9 M_\odot$ host an MBH seed, regardless of the J_{crit} threshold.

width $\log_{10} M/M_{\odot} = 0.5$ that host at least one MBH.

In Figure 2.5 we investigate the effect of varying J_{crit} thresholds on the MBH occupation fraction at the end of our simulations. Even under the most stringent formation criteria, a minimum of 50% of halos with masses larger than $3 \times 10^9 M_{\odot}$ at $z = 5$ host at least one MBH. These halos are expected to grow to be highly massive ($10^{11} - 10^{12} M_{\odot}$) by the present day (McBride et al., 2009). The difference between these thresholds is most apparent below $\sim 3 \times 10^8 M_{\odot}$, arguing that the occupation fraction of Milky Way-mass disk galaxies at redshift zero may inform $J_{\rm crit}$. Mapping local occupation fraction to high redshift is more complicated in general but far more so for low mass galaxies, where gravitational wave recoil and alternative seed formation channels may become increasingly important (Schnittman & Buonanno, 2007; Blecha & Loeb, 2008; Holley-Bockelmann et al., 2008, 2010). Incorporating these effects in a statistical sense may require a close collaboration between state-of-the-art simulations like these and semi-analytic techniques.

2.4.2 Sources of Lyman-Werner radiation

Primordial star formation is thought to provide the essential Lyman-Werner flux to spur direct collapse black hole formation, but the proximity to these star formation sites is not well-constrained. One favored model of isothermal direct collapse invokes the synchronized growth of a pair of neighboring atomic cooling halos (Dijkstra et al., 2008; Visbal et al., 2014b). As one of the halos crosses the atomic cooling threshold, it experiences a burst of star formation that irradiates the secondary neighbor. If the Lyman-Werner radiation generated by this stellar population is sufficient, it prevents molecular hydrogen cooling in the secondary halo, setting up the right conditions for direct collapse.

We investigate the proximity and synchronization of Lyman-Werner sources and direct collapse sites to characterize the types of scenarios that favor direct collapse. Since the

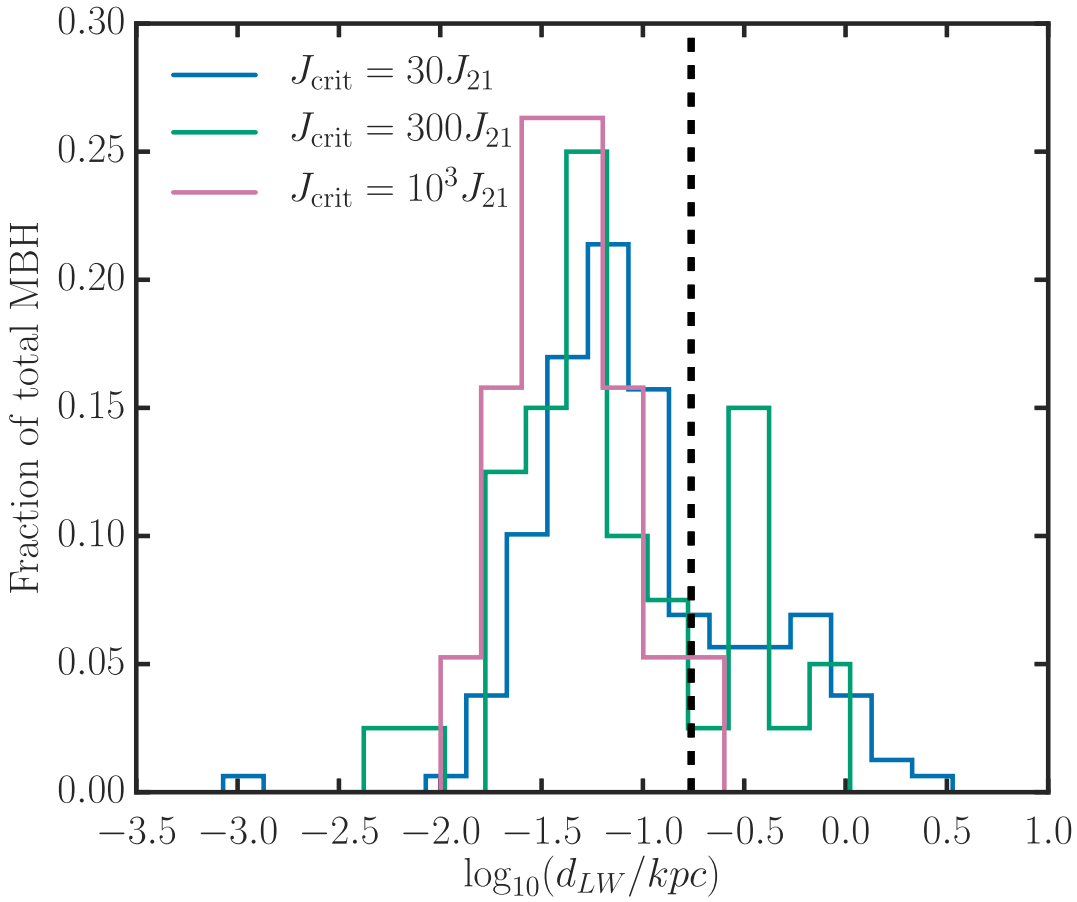

Figure 2.6: MBH-LW SOURCE SEPARATIONS Distributions of distances between MBH formation sites and the estimated dominant source of LW radiation. The dashed vertical line marks one softening length. For most MBHs, the nearest source of LW radiation is located inside the host halo and less than one softening length from the MBH formation site.

strength of Lyman-Werner flux scales as $\sim d^{-2}$, we approximate the dominant source of Lyman-Werner radiation for each MBH seed as the nearest star forming region that formed prior to seed formation. To demonstrate the validity of this assumption, we provide some examples here. At $z = 24$ in the $J30$ simulation, an MBH forms in a $2 \times 10^7 M_\odot$ halo. The dominant source of Lyman-Werner radiation is a star particle that formed in this halo less than 1 Myr before the MBH seed and 0.5 kpc from the direct collapse site. The flux from this starforming region is six orders of magnitude larger than the flux from the only other starforming region at this time, which is ~ 50 kpc away, and has triggered direct collapse in its own halo.

As the simulation evolves and star formation increases, more distant starforming regions begin to contribute a more significant fraction of the total Lyman-Werner flux on the direct collapse sites. At $z = 10$ in the $J30$ simulation, an MBH forms in a $2 \times 10^8 M_\odot$ halo that previously formed one star particle approximately 1 kpc from the direct collapse site. The Lyman-Werner flux from this single star particle comprises $\sim 75\%$ of $J_{\rm crit}$ while the remainder of the supplemental flux comes from a neighboring starforming halo ~ 75 kpc away, bringing the total Lyman-Werner flux at the direct collapse site above $J_{\rm crit}$.

In Figure 2.6, we show the distance from MBH seed formation sites to the nearest star particle. We find that $\gtrsim 80\%$ of the irradiating sources are inside the same halo and less than 2 kpc away from the radiation source. MBH seeds in these simulations form in pockets of low-metallicity gas that are exposed to Lyman-Werner radiation from star forming regions within their host halos. With lower $J_{\rm crit}$ thresholds, MBH seeds are able to form at larger distances from Lyman-Werner sources and farther from the centers of the host halos.

We do notice synchronization between star and MBH seed formation within the same halo; regardless of $J_{\rm crit}$, the majority of Lyman-Werner sources formed less than 5 Myr before the collapse of their respective MBH pairs. This contemporaneity of MBH seeds and nearby stars hints at a tendency for Lyman-Werner sources and MBHs to form in synchronized pairs, as predicted by Dijkstra et al. (2008); Visbal et al. (2014b), although

the pairs that we find in these simulations tend to form in a single halo. In this scenario, stars form and a MBH seed forms shortly afterwards before metals can contaminate the halo. In the $J30$ simulation, we observe a single instance of seed formation that closely resembles the atomic cooling halo pair scenario, which we illustrate in Figures 2.7 and 2.8. This scenario is quite similar to that proposed in Visbal et al. (2014b). At $z = 13$, a halo of mass $2.5 \times 10^8 M_\odot$ crosses the virial radius and becomes a subhalo of a more massive halo ($8 \times 10^8 M_\odot$). While the subhalo remains pristine, the more massive parent halo begins forming stars, providing enough Lyman-Werner radiation to form five MBH seeds in the subhalo. From this one example, we conclude that while atomic cooling pairs are a viable seed formation mechanism in general, it is too rare to comprise the bulk of the seed formation in our models. Alternatively, we show that direct collapse black holes can, and predominantly do, form in low-metallicity pockets of halos with prior star formation.

2.4.3 Characteristics of halos that host MBH seeds

The canonical picture of direct collapse allows a single MBH seed to form in a globally pristine halo with no history of star formation. In contrast, our simulations indicate that this process is significantly more complex and should be treated as such. This complexity could be expected by considering the more complicated way realistic halos form and evolve. Even immediately after a halo forms, it is not spherically symmetric or homogeneous, but exhibits irregular morphology. Likewise, gas collapse is not monolithic, but rather clumpy and stochastic. Conditions inside these dark matter halos can be ripe for both star formation and direct collapse within a single halo, and may produce multiple MBH seeds. In this set of simulations, it is not uncommon for MBHs to form in groups that quickly merge to form a more massive MBH. Since we have taken precautions to prevent spurious MBH formation, as discussed in Section 2.3, we believe the formation of multiple MBH seeds per halo is a real result, and not a numerical effect.

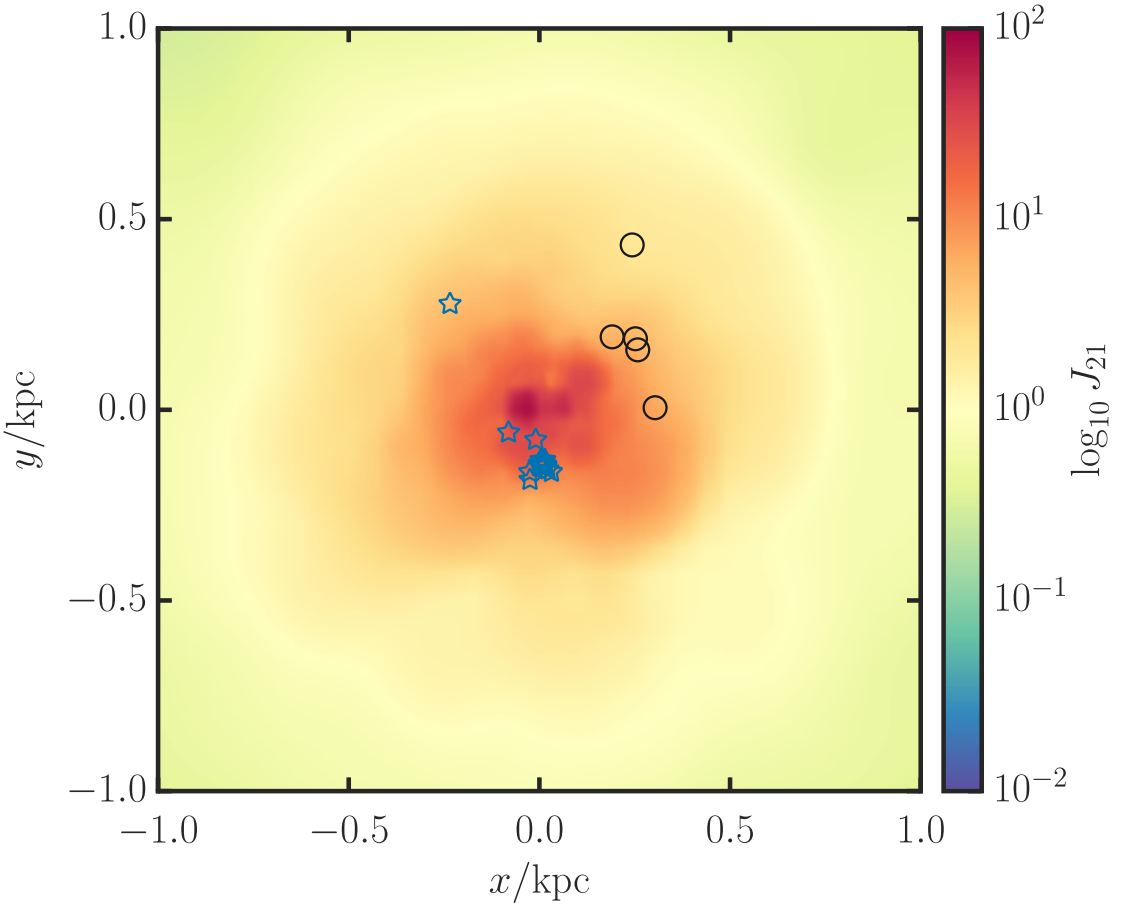

Figure 2.7: AN ATOMIC COOLING HALO PAIR CANDIDATE Massive black hole seed positions are marked by black circles in this $z = 13$ line-of-sight averaged Lyman Werner flux image of the atomic cooling halo pair candidate in the $J30$ simulation. The five MBH seeds are members of the $2.5 \times 10^8 M_\odot$ subhalo that has not formed stars. Blue stars mark the positions of nearby star particles, which are members of the $8 \times 10^8 M_\odot$ parent halo.

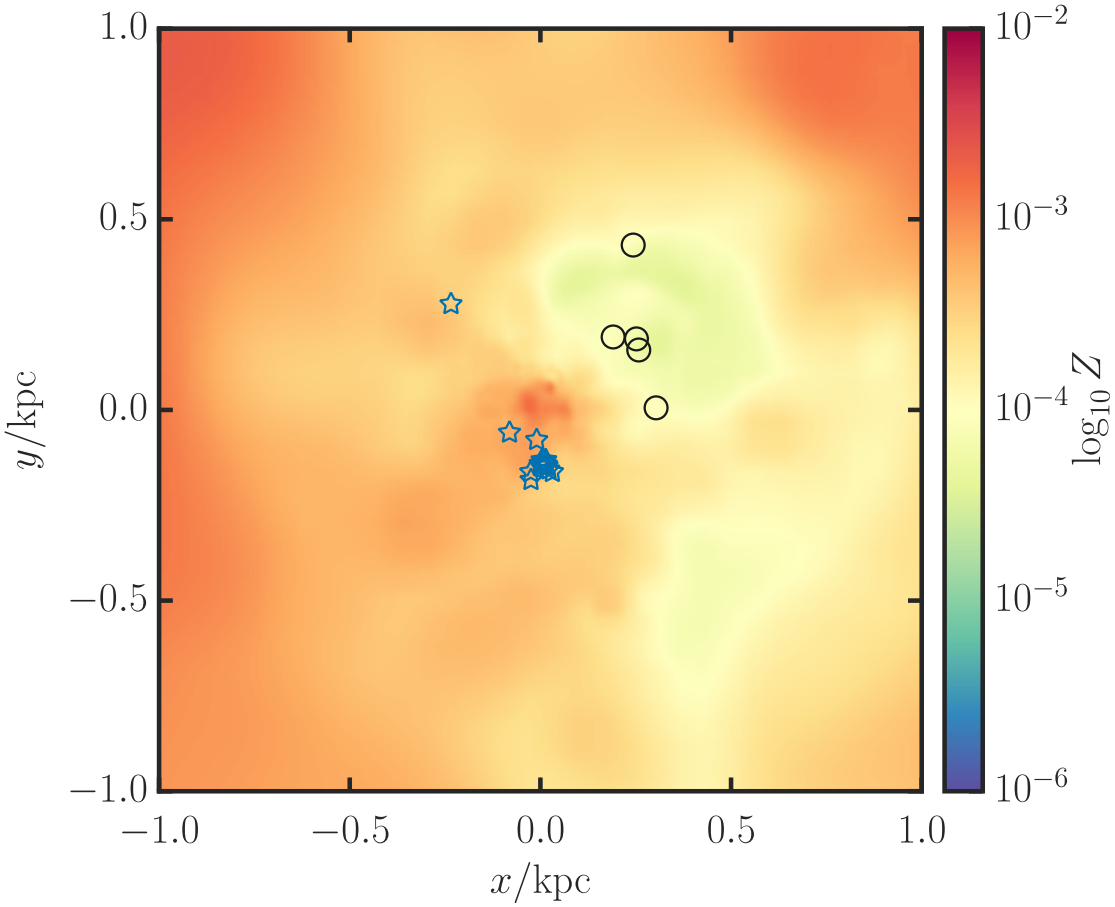

Figure 2.8: AN ATOMIC COOLING HALO PAIR CANDIDATE MBH and star particle positions are marked in a line-of-sight averaged metallicity image of the atomic cooling halo pair candidate. MBH seeds form in regions that experience high Lyman-Werner flux but are still sufficiently metal poor.

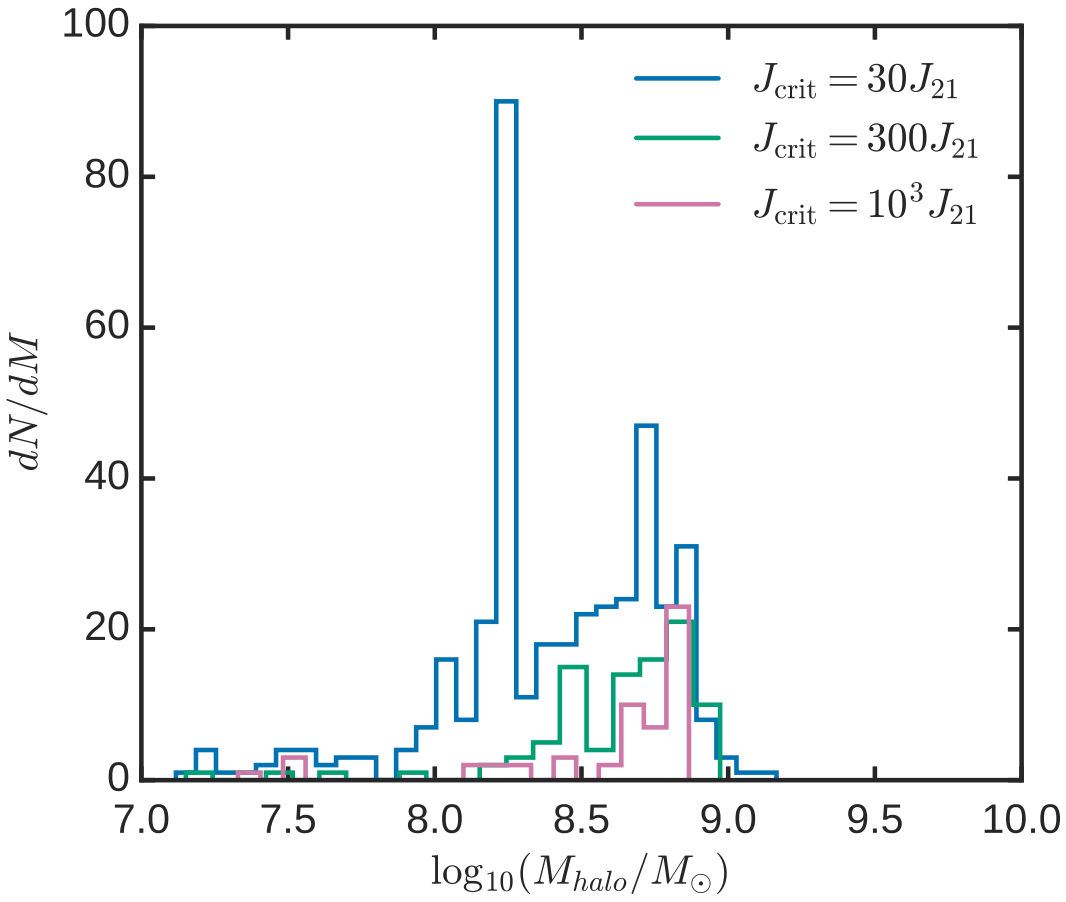

Figure 2.9: MASSES OF MBH-FORMING HALOS A distribution of halo masses at the time of MBH seed formation in each simulation show that MBHs form preferentially in halos with masses greater than $10^8 M_\odot$.

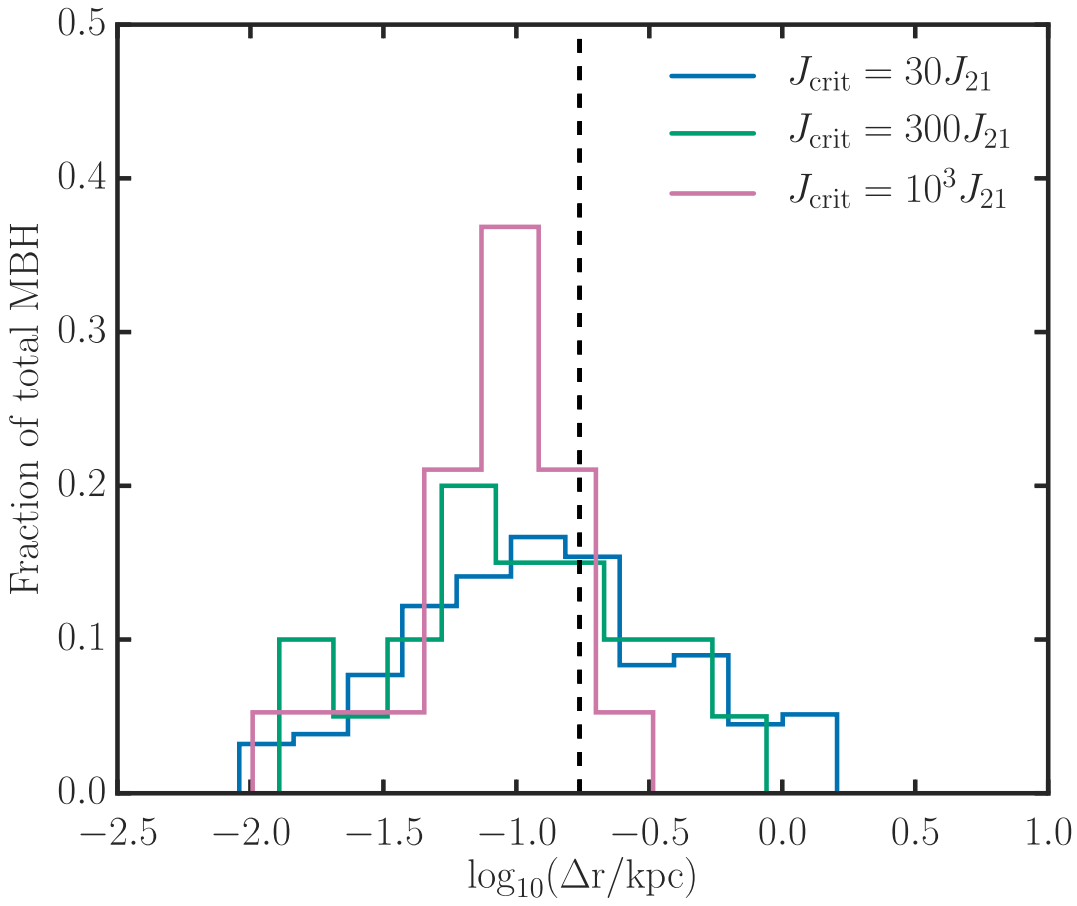

Figure 2.10: MBH-HOST HALO CENTER SEPARATIONS Distributions of offsets between MBH formation sites and host halo centers of mass. The dashed vertical line marks one softening length. Most MBHs form within one softening length of the host halo's center of mass.

In Figure 2.9 we show the masses of seed host halos at the time of seed black hole formation in our three simulations. While we do not explicitly constrain the halo masses of potential seed hosts, the minimum gas density threshold we set effectively acts as a proxy for preferential MBH formation in more massive halos. Similarly, while there are no explicit restrictions placed on where in the halo an MBH can form, the densities required to form an MBH create a natural tendency for direct collapse to occur at the centers of the host halos. In Figure 2.10, we show the distributions of offsets between the MBH formation site and the host halo center-of-mass. The majority of MBHs form within one softening length of the center of the host halo.

In a comparison of global halo characteristics of halos that host MBHs and those that do not, we find a slight decrease in the mean halo concentration of MBH-hosting halos as compared to the mean halo concentration of all halos. While this trend persists at all redshifts, it is not statistically significant.

2.5 Summary

In this work, we used cosmological simulations to study the formation of direct collapse MBH seeds under the influence of of spatially and temporally varying anisotropic Lyman-Werner radiation field and characterize the demographics of MBH formation sites. In future work, we will examine MBH seed formation and early growth in a larger suite of simulations spanning $z = 0$ halo masses from dwarfs to massive elliptical galaxies.

Building on the findings of Bellovary et al. (2011), that MBH seeds can form in less massive halos, we additionally find that direct collapse MBH seeds can form in halos with star formation history and non-zero metallicity. Lower $J_{\rm crit}$ values allow MBH seeds to form more abundantly, at lower redshifts, and in less massive halos. The sources of H_2 dissociating Lyman-Werner photons are likely to form in the same halo as the seed. We

have shown that, contrary to the canonical model, MBHs do not need to form singly in completely pristine halos. This work indicates that conditions favorable for MBH formation may necessitate some previous star formation in the host halo, thereby causing MBHs to form in metal-enriched halos. Multiple MBHs can, and do, form in a single halo, and these black holes often merge into larger seeds.

The limitations of this work stem from the challenge of incorporating physical processes that occur across large dynamic ranges in cosmological simulation. The occupation fractions presented in this paper are upper limits because we do not account for gravitational recoil, which will cause some fraction of MBHs to evacuate their halos when merging. We are not able fully resolve the collapse of gas into a MBH seed, which occurs on sub-parsec scales, and instead must represent this unresolved physics with sub-grid models that take as input the conditions of the gas physics at distances of $\sim$ 100s of parsecs. Another source of uncertainty is the Lyman-Werner escape fraction, which depends of the form of propagation of the ionization front (Schauer et al., 2017a). To correctly compute exact Lyman-Werner fluxes would require a full treatment of radiative transfer. These simulations also do not account for X-ray radiation, which alters the gas chemistry by increasing the free electron fraction, thereby inciting H_2 formation (Haiman et al., 1996; Haiman & Loeb, 2001; Tanaka et al., 2012).

There are currently very few observational constraints on MBH formation, high-redshift occupation fractions, or MBH-MBH merger rates. Future electromagnetic and gravitational wave observatories, including JWST, LISA, ATHENA, LUVOIR and LYNX, may offer some of the first chances to observationally constrain MBH formation scenarios. LISA, specifically, is the only mission that will be able to observe MBH-MBH mergers out to $z \sim 20$, and so will uniquely observe the seed formation epoch directly (Amaro-Seoane et al., 2017). We can track the expected gravitational strain amplitude of each MBH-MBH merger to predict the total stochastic gravitational wave signal from the population of MBH-MBH mergers as a function of time (e.g., Holley-Bockelmann et al., 2010); this will provide

a foundation for LISA observations to constrain MBH formation. In a future paper, we will calculate the gravitational wave signal from early MBH seed mergers and discuss the potential detectability of these events with LISA.

Chapter 3

The role of mergers in the assembly of massive black hole seeds

This chapter will be submitted to The Astrophysical Journal in collaboration with Kelly Holley-Bockelmann and Jillian Bellovary. It appears here with minor formatting changes.

When two black holes merge, the asymmetric emission of gravitational waves provides an impulse to the merged system; this gravitational wave recoil velocity can be up to 4000 km/s, easily fast enough for the black hole to escape its host galaxy. We combine semi-analytic modeling with cosmological zoom-in simulations of a Milky Way-type galaxy to investigate the role of black hole spin and gravitational recoil in the epoch of massive black hole seeding. We sample four different spin distributions (random, aligned, anti-aligned, and zero spin), and compare the resulting merger histories, occupation fractions, and MBH-host relations with what is expected by excluding the effect of recoil. The inclusion of gravitational recoil and MBH spin in the assembly of MBH seeds can reduce the final $z = 5$ MBH mass by up to an order of magnitude. The MBH occupation fraction, however, remains effectively unaltered due to episodes of black hole formation following a recoil event. While electromagnetic detections of these events are unlikely, LISA is ideally suited to detect gravitational wave signals from such events.

3.1 Introduction

By now, massive black holes (MBH) are a well-established galaxy component found in an astonishing variety of galaxy hosts, from bulgeless spirals (Satyapal et al., 2009; Araya Salvo et al., 2012; Simmons et al., 2013, 2017), low-surface brightness galaxies (Subramanian et al., 2016), and dwarfs (Reines et al., 2011; Baldassare et al., 2018; Secrest et al., 2015; Marleau et al., 2017; Mezcua et al., 2018) to the brightest cluster ellipticals (McConnell et al., 2012; Ferré-Mateu et al., 2015), and at a wide range of redshifts (Bañados et al., 2018). These MBHs must have formed within the first billion years of the Universe and likely to the form of massive 'seed' black holes (Haiman & Loeb, 2001) via the remnants of Population III stars (Madau & Rees, 2001; Johnson & Bromm, 2007; Xu et al., 2013) (see, however Smith et al. (2018)) or direct collapse (Loeb & Rasio, 1994; Koushiappas et al., 2004; Begelman et al., 2006; Lodato & Natarajan, 2006; Haiman, 2006; Spaans & Silk, 2006).

Observations of the local Universe describe a correlation between the mass of the central black hole and the velocity dispersion of the bulge component of the host galaxy, commonly known as the $M_{\rm BH} - \sigma$ relation (Gebhardt et al., 2000; Ferrarese & Merritt, 2000; Tremaine et al., 2002; Gültekin et al., 2009; McConnell & Ma, 2013; Kormendy & Ho, 2013; Woo et al., 2013; Saglia et al., 2016). Related MBH-host scaling relations abound, including $M_{\rm BH} - M_{\rm bulge}$, $M_{\rm BH} - L_{\rm bulge}$, $M_{\rm BH} - M_{\rm stellar}$, and $M_{\rm BH} - M_{\rm halo}$ (see e.g., Kormendy & Ho, 2013). An MBH and its host halo co-evolve as a system, and there is a wealth of literature exploring how this relationship can be harnessed to understand galaxy formation (Di Matteo et al., 2008; Micic et al., 2007; Barausse, 2012; Antonini et al., 2015) and MBH demographics (e.g., Merritt & Ferrarese, 2001; Micic et al., 2008; Volonteri & Natarajan, 2009; Tremmel et al., 2017; Heckman & Best, 2014).

Any MBH-host co-evolutionary model, however, must contend with MBH binary dynamics, such as three-body scattering, gravitational wave emission, and gravitational wave recoil (Merritt & Milosavljević, 2005). Gravitational recoil is caused by the anisotropic

emission of gravitational radiation during a merger of two compact objects (Bekenstein, 1973). As MBHs merge, asymmetries in the merger configuration cause an asymmetric gravitational wave emission pattern. This, in turn, radiates linear and angular momentum in a preferred direction, which imparts a gravitational kick to the merged object to conserve momentum. This kick can range up to 5000 km/s (Campanelli et al., 2007b; Lousto & Zlochower, 2011), with the high velocity 'superkick' tail caused by spins anti-aligned to one another, perpendicular to the orbital plane and highly eccentric (González et al., 2007; Campanelli et al., 2007b; Herrmann et al., 2007; Baker et al., 2008), and even larger kicks occurring for partially aligned spins in certain 'hangup' configurations (Lousto & Zlochower, 2011). More typical recoil velocities are of order a hundred km/s for circular orbits, low spins, and aligned spin configurations (Campanelli et al., 2007a).

The magnitude of these kick velocities presents a challenge to our simple picture of central black hole evolution. Low mass halos and globular clusters, for example, cannot retain seed MBHs suffering even mild kicks (Volonteri, 2007; Holley-Bockelmann et al., 2008). Indeed, recoil velocities likely exceed the escape velocities of all but the most massive host halos, ejecting the new MBH from its host (Micic et al., 2006, 2011; Sijacki et al., 2009; Gerosa & Sesana, 2015; Blecha et al., 2016; Kelley et al., 2017). Even moderate kicks can eject a MBH from high$-z$ galaxies, when halo virial masses are still small and halos lack sufficiently deep potential wells to retain these merged objects (Merritt et al., 2004; Micic et al., 2011; Schnittman & Buonanno, 2007; Volonteri, 2007). Gravitational recoil may be responsible for a population of wandering black holes in the halos of galaxies (Libeskind et al., 2006; Micic et al., 2011), though these are also expected from long dynamical friction sinking timescales (Bellovary et al., 2010; Micic et al., 2011). MBHs kicked at velocities that approach, but do not exceed, the escape velocity of the host, may oscillate on large orbits unless the host is gas rich, in which case gas exerts drag on the MBH and restricts its orbit to the central region of the host galaxy (Blecha et al., 2011; Guedes et al., 2011).

By displacing the MBH, gravitational wave recoil can significantly alter the co-evolution

of an MBH and its host. Outside the gas-rich center, MBH growth is stifled and the resulting low mass accretion interrupts the AGN feedback process (Blecha & Loeb, 2008; Sijacki et al., 2009). Without a central MBH to fuel, the gas can instead form stars and build up a bulge (Blecha et al., 2011), which can have profound effects on MBH scaling relations. Recoil velocities may, however, be low in gas-rich environments: if MBH-MBH mergers occur as a result of galactic mergers, torque due to gas accretion may force the MBH spin axes to align with that of the galactic disks, leading to lower recoil velocities and consequently a retention of MBHs at the centers of host galaxies after the merger (Bogdanović et al., 2007; Barausse, 2012; Dotti et al., 2010; Blecha et al., 2016).

Recoil events are likely to be suppressed in gas-rich environments, largely because the magnitude of recoil velocities depend on the spin configuration of the binary system prior to the merger (Campanelli et al., 2007b), and accretion can force the spins of an MBH binary to align (Bogdanović et al., 2007; Barausse, 2012), resulting in minimal kicks (Dotti et al., 2010). As has been shown previously and will be demonstrated again in this work, gravitational recoil velocities produced by the merger of two MBHs with aligned spins are significantly smaller than that of anti-aligned or randomly oriented spins. If MBH-MBH mergers occur as a result of galactic mergers, torque due to gas accretion may force the MBH spin axes to align with that of the galactic disks, leading to lower recoil velocities and consequently a retention of MBHs at the centers of host galaxies after the merger (Bogdanović et al., 2007; Blecha et al., 2016). Though circumbinary gaseous disks may provide the conditions necessary to align the spins of two merging black holes via the Bardeen-Petterson effect, rapidly spinning black holes may not have sufficient time to align, and therefore remain subject to large recoil velocities (Lodato & Gerosa, 2013).

The purpose of this work is to study the effect of gravitational recoil due to MBH-MBH mergers during the early assembly of MBH seeds. We follow MBH seeds formed via direct collapse (Dunn et al., 2018) as they co-evolve with their host halos and merge with other MBHs. In this paper, we investigate how gravitational recoil affects the high redshift

MBH mass function, merger rate, occupation fraction and MBH-host scaling relations. Since MBH seeds are thought to be sown in the pre-reionization era, it may seem that the impact of recoil would be all but impossible to observe. However, the gravitational waves generated from MBH mergers are the loudest known source in the Universe and easily penetrate through matter, opening a gravitational window onto the cosmic dawn. The Laser Interferometer Space Antenna (LISA), for example, is specifically designed to detect seed black hole mergers that may spawn the first quasars, translating into an observational requirement to detect the coalescence of MBHs in the mass range of $10^3 - 10^5 M_\odot$ between redshifts $10-15$ and $10^4 - 10^6 M_\odot$ at redshifts greater than 9, with signal-to-noise ratios in the hundreds (Amaro-Seoane et al., 2017). With the advent of LISA, gravitational recoil kicks larger than ~ 500 km/s may even be directly observable through a Doppler shift of the gravitational wave signal during ringdown (Gerosa & Moore, 2016). The proposed X-ray flagship observatory, Lynx, is designed with high throughput and fine angular resolution to observe highly accreting seed black holes at such high redshifts, as well. The synergy between LISA and Lynx could give us the opportunity to construct MBH seed demographics and follow complementary channels of seed growth (Colpi et al., 2019).

This Chapter is organized as follows: in Section 3.2, we describe the simulations that were used to generate the MBH merger tree; in Section 3.3 we discuss the semi-analytic gravitational recoil model; and in Section 3.4, we discuss the importance of incorporating gravitational recoil into models that make predictions about the assembly of MBH seeds and the relationships between MBHs and their host galaxies.

3.2 Simulations

Our study is based on simulations using the N-body+Smooth Particle Hydrodynamics (SPH) tree code GASOLINE (Stadel, 2001; Wadsley et al., 2004, 2017), which study the

evolution of MBH seeds in cosmological zoom-in simulations. We simulated the formation of a redshift zero Milky Way-mass halo until $z = 5$, employing physically motivated prescriptions for black hole formation, accretion, feedback and mergers (Bellovary et al., 2010; Dunn et al., 2018). MBHs in these simulations form from dense, converging, low-metallicity gas particles experiencing Lyman-Werner specific intensity above a criticial threshold, $J_{\rm crit}$, which we vary from 30 to $10^3 J_{21}$. When an MBH forms, it subsumes the mass of its parent gas particle, forming with a mass of $2 \times 10^4 M_\odot$. For a detailed description of the simulations that generated the data used in this paper, see Section 2 of Dunn et al. (2018).

One of the major findings from our previous work was that multiple MBH seeds can form in a single halo in sequential bursts. These multiples form despite concerted efforts to prevent spurious MBH overproduction. No two MBH seeds are not permitted to form at the same time step within two softening lengths of each other. If more than one gas particle meets the MBH formation criteria within this volume at the same time step, only the most bound particle becomes an MBH seed, and the remaining MBH candidates revert to their parent gas particles. Even with this restriction, the multiplicity of MBH seeds forming within small volumes of space and windows of time leads to MBH-MBH mergers. We repurpose the $J_{\rm crit} = 10^3 J_{21}$ simulation here to investigate the role of mergers in MBH assembly. Of the three simulations in this suite, this $J_{\rm crit}$ invokes the most strict MBH formation recipe, resulting in the lowest MBH formation efficiency.

We note here that the possibility of forming more that one direct collapse black hole seed per halo is controversial. One strong impediment to multiple seeds is the rate of gas inflow required by direct collapse, which must exceed $0.1 M_\odot/\mathrm{yr}$ for $\sim 1 - 10$ Myr (Hosokawa et al., 2013; Alexander & Natarajan, 2014; Umeda et al., 2016). It may be difficult for this rapid collapse to occur at multiple locations or multiple occasions in a single halo. Additionally, the separations between a direct collapse host halo and a neighboring star forming halo may need to be finely tuned to provide the necessary Lyman-Werner radiation without subjecting the MBH-forming halo to tidal disruptions (Chon et al., 2016). However,

this work, like all simulations, is limited by its resolution, and MBH and star formation in GASOLINE simulations are designed to rely only on local gas physics. Furthermore, since the Lyman-Werner sources in Dunn et al. (2018) are nearly exclusively *internal* to the the direct collapse host halo, this configuration may allow Lyman-Werner radiation to reach the direct collapse site without the threat of tidal disruption.

3.3 Semi-analytic modeling

In Gasoline, MBH seeds can grow through mergers, when two sink particles are less than two softening lengths apart and their relative velocities are small: $\frac{1}{2}\Delta\vec{v}^2 < \Delta\vec{a}\cdot\Delta\vec{r}$, where $\Delta\vec{v}$ and $\Delta\vec{a}$ are the differences in velocity and acceleration of the two black holes, and $\Delta\vec{r}$ is their separation. Our GASOLINE simulations do not include gravitational recoil due to MBH mergers. To incorporate gravitational recoil into the simulations in post-processing, we follow the work of Schnittman & Buonanno (2007) to construct a semi-analytic model of gravitational recoil events based on MBH interactions in the simulation. The empirical expression for the total sum of recoil velocities described in Campanelli et al. (2007a) is based on the post-Newtonian expression for linear momentum lost to gravitational radiation during a merger of spinning, unequal mass black holes. The authors demonstrate that recoil velocities are dominated by the spin contribution, and construct an empirical formula that sums the contributions of mass and parallel and perpendicular angular momentum components.

This heuristic formula depends on the mass ratio q, the specific spin magnitudes α_1 and α_2, and the angle Θ between the in-plane spin component and the infall direction (Campanelli et al., 2007a):

$$V_{recoil}(q,\alpha) = v_m + v_\perp + v_{||} \tag{3.1}$$

$$v_m = A\frac{q^2(1-q)}{(1+q)^5}1 + B\frac{q}{(1+q)^2} \tag{3.2}$$

$$v_\perp = H\frac{q^2}{(1+q)^5}(\alpha_2^{||} - q\alpha_1^{||}) \tag{3.3}$$

$$v_{||} = K\cos(\Theta)\frac{q^2(1-q)}{(1+q)^5}(\alpha_2^{\perp} - \alpha_1^{\perp}) \tag{3.4}$$

where $A = 1.2 \times 10^4$ km/s, $B = -0.93$, and $H = 7.3 \times 10^3$ km/s. We construct four MBH merger history models to compare with the 'no kick' model from our original simulation: no spin ($\alpha_1 = \alpha_2 = 0$), random spins ($-1 < \alpha_{1,2} < 1$; $0 < \Theta < \pi$; $\alpha_1 \neq \alpha_2$), aligned spins ($\alpha_1 \neq \alpha_2$; $\Theta = 0$), and anti-aligned spins ($\alpha_1 \neq \alpha_2$; $\Theta = \pi$). The mass ratios used in these models are drawn from the fiducial simulation, while the spin amplitudes and orientations are drawn from a random distribution. The orientations of the aligned and anti-aligned spins are in the plane of the binary orbit. We run 100 Monte Carlo trials of each spin model, and summarize some aspects of the MBH populations produced by these models in Table 3.1.

Recoil model	$N_{\rm mergers}$	$N_{\rm ejections}$	$\max(M_{BH}/M_\odot)$ at $z = 5$	$Q_1(M_{BH}/M_\odot)$ at $z = 5$	$Q_3(M_{BH}/M_\odot)$ at $z = 5$
No kick	45	0	4×10^5	2.7×10^4	1.1×10^5
No spin	35	15	1.1×10^5	2.7×10^4	5.4×10^4
Random spins	29	25	4.6×10^4	2.7×10^4	3.7×10^4
Aligned spins	35	14	1.1×10^5	2.7×10^4	3.9×10^4
Anti-aligned spins	28	26	4.5×10^4	2.7×10^4	3×10^4

Table 3.1: SIMULATION PARAMETERS Summary of selected results of the simulations presented in this paper. (1) Spin distribution model, (2) Total number of mergers, (3) Number of merged MBHs that are ejected from their host halo, (4) Mass of the largest MBH at $z = 5$, (5) First quartile (25^{th} percentile) of MBH masses at $z = 5$, (6) Third quartile (75^{th} percentile) of MBH masses at $z = 5$. Values for the aligned, anti-aligned, and random spin distributions are averaged results of 100 iterations of the merger history.

3.4 Results

There is a marked change in the numbers of mergers and ejections, as well as the final MBH masses, with the incorporation of any recoil model (Table 3.1). The random spin and anti-aligned spin recoil models yield the most drastic difference in the $z = 5$ MBH populations, as they generate larger recoil velocities. Here we discuss some ways that incorporating gravitational recoil events into the MBH assembly history changes the MBH population predicted by our simulations.

The occupation fraction of MBHs likely encodes information about the details of MBH formation and early assembly. We define the MBH occupation fraction as the fraction of halos in a mass bin that host at least one MBH. In Figure 3.1, we show the resulting MBH occupation fraction at $z = 5$ for each of our recoil models. Incorporation of recoil and spin into the MBH merger tree does yield a reduction in MBH occupation fraction. However, the discrepancies between the predicted occupation fractions for the different spin recoil models are not larger than the errors associated with the measurements, and therefore not statistically significant. The error bars on the fiducial 'no kick' model and the 'no spin' model represent the Poisson error, since these models require no randomly-generated component in the calculation of the recoil velocity. The occupation fractions of the three remaining spin-recoil models, which do require randomly selected components to compute recoil velocities, are averaged over 100 Monte Carlo trials. Note that the error bars on these occupation fractions therefore encompass both Poisson error and random error.

When gravitational recoil is included, multiple bursts of MBH formation in these simulations effectively refill host halos from which merged MBHs were previously ejected. These refill events prevent the depletion of MBH host halos, and thereby prevent a drastic reduction of the MBH occupation fraction. As discussed in Dunn et al. (2018), our MBH formation recipe does not prevent more than one MBH seed from forming per halo, though we do take measures to prevent the spurious overproduction of MBH seeds in a single time step within a volume enclosing two softening lengths. As a result, a single halo can

experience multiple sequential episodes MBH formation. Without gravitational recoil, as represented by our 'no kick' model, MBHs that form in the same host halo merge to form a more massive seed by $z = 5$.

The changes in the shape of the occupation fraction in Figure 3.1 are determined by the fraction of mergers with recoil velocities greater than the host halo escape velocity. In Figure 3.2, we compare the distributions of recoil velocities generated by different recoil models to the distribution of host halo escape velocities. The distribution of host halo escape velocities is shown in solid grey, with a mean and median escape velocities of 43 km/s and 47 km/s, respectively. The recoil velocities largely tend to be either orders of magnitude smaller or larger than the the escape velocities of the host halos, which themselves only span a single order of magnitude. The random spin and anti-aligned spin recoil models are generally associated with kick velocities greater than or equal to the escape velocities of the host halos, nearly always resulting an ejection. Otherwise, the 'no spin' and aligned spin recoil models generate velocities spread over a larger range of magnitudes, and are less likely to be ejected. Since halos are still quite small at these high redshifts, the recoil velocities can be comparable to, or significantly larger than, the halo escape velocities. In turn, it is important to consider the effects of recoil in our simulations because our assumptions about MBH escape fractions and merged masses will leave an imprint on the predicted observables.

While the focus of this work is recoil events that fully eject MBHs from the host halo, recoil events that cause MBHs to reach velocities that are a significant fraction of the host halo escape velocity are likely also important to the mass assembly of the MBH. Recoil events for which the recoil velocity is larger than the host halo escape velocity are will eject the MBH from the halo. In scenarios where the recoil velocity is a significant fraction of the host halo escape velocity, the MBH is likely kicked out of the central region of the halo and then 'sloshes' back towards the center of the halo. This motion may play an important role in regulating the growth of the black hole. As the MBH wanders throughout the host halo, its motion can prevent capture into another binary system (Guedes et al., 2011), and stifle

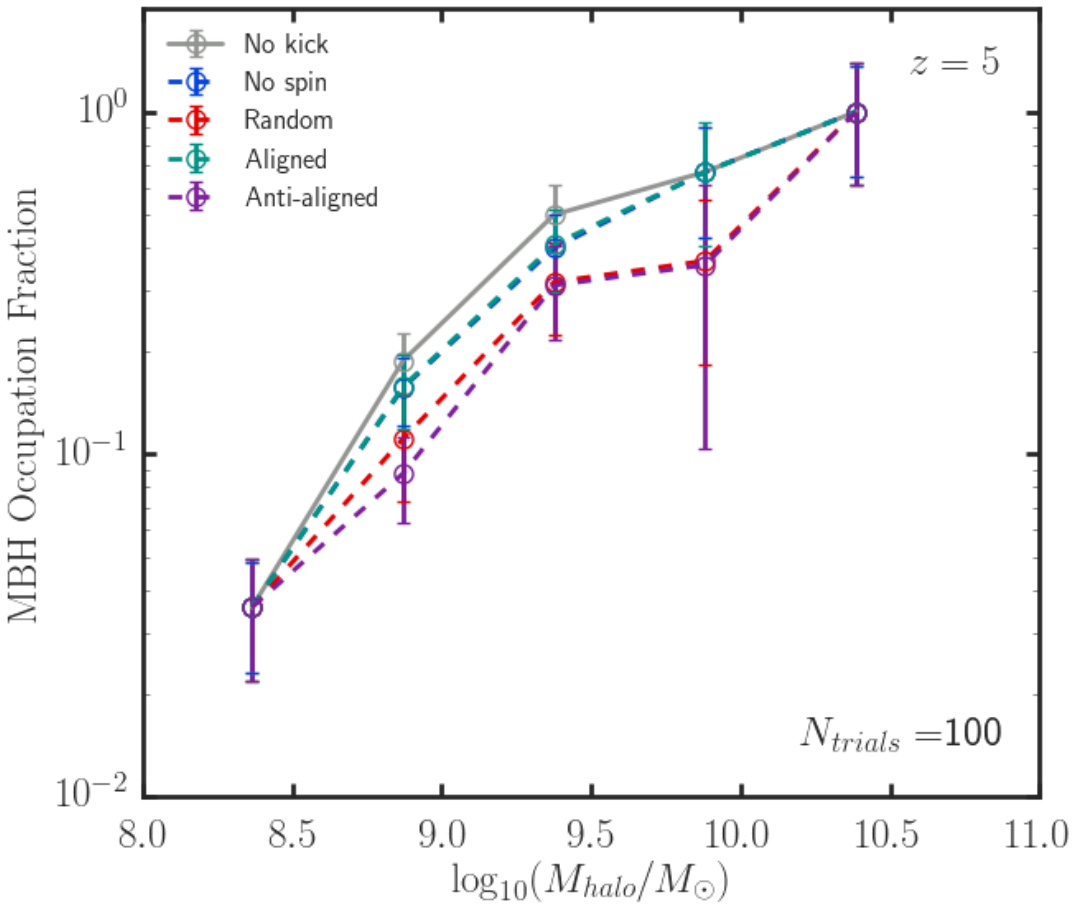

Figure 3.1: OCCUPATION FRACTIONS MBH occupation fractions for different spin distributions at $z = 5$. MBH occupation fractions computed for the random, aligned, and anti-aligned spin configurations are averaged over 100 trials. The error bars on the 'no kick' and 'no spin' models represent the Poisson error, whereas the error bars for the remaining models represent contributions from both Poisson error and random error. While the MBH occupation fraction appears smaller for the random spin and anti-aligned spin distributions, these differences are not statistically significant. The MBH occupation fraction remains similar to its fiducial value even with gravitational recoil ejections because multiple epochs of MBH formation can refill an empty host halo.

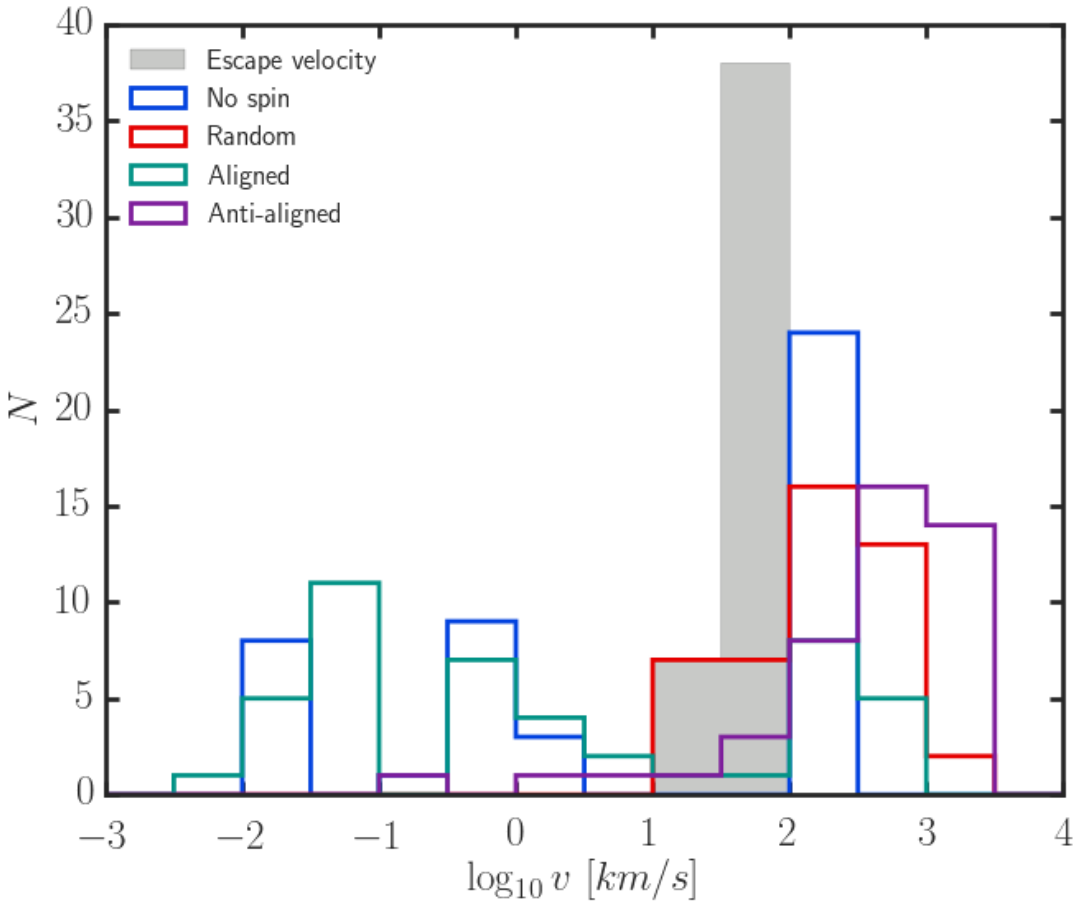

Figure 3.2: VELOCITY DISTRIBUTIONS We compare the distribution of escape velocities of host halos, shown in grey, with the distributions of recoil velocities in each of the spin configuration models, shown in their corresponding colors (see legend). In general, the recoil velocities are either much smaller or much larger than the escape velocities, which only span one order of magnitude.

growth through limited gas accretion (e.g., Blecha & Loeb, 2008). Since our simulations do not resolve dynamical friction, we are not able to fully model the orbit of such MBHs. However, we can note that recoil events in the 'no spin' and aligned-spin models are unlikely to be kicked far from their original locations due to an MBH merger, whereas recoil events in the random spin and anti-aligned spin models are more likely to be displaced from their original locations, due to their large kick velocities.

One commonly accepted idea about MBH-MBH mergers is that they are preceded and triggered by galaxy mergers. In our simulations, MBH-MBH mergers also happen in a single halo as a direct result of the formation of multiple MBH seeds in that halo. In Figure 3.3, we show the number of mergers as a function of redshift in each of our models. We emphasize here that this figure shows merger histories, not merger rates. Since this work uses zoom-in simulations, we do not generate a statistical sample that would be necessary to calculate the rate of MBH mergers that may be observable with LISA. The redshift distribution of MBH-MBH mergers closely mirrors that of MBH formation, shown in black. The number of black hole mergers in the original simulation, with no recoil model, is shown by the filled gray bars. Each of the four gravitational recoil models decrease the number of black hole mergers in the assembly history of this galaxy. The MBH-MBH mergers that we recover in this simulation are a direct result of the formation of multiple MBH seeds within small volumes of space and windows of time. This indicates that some of the mergers detected by LISA may be of black holes that recently formed in a single halo and are still very close to the original seed mass.

Gravitational recoil events likely contribute to the intrinsic scatter in MBH-host scaling relations (Libeskind et al., 2006; Volonteri, 2007; Devecchi et al., 2009). In Figure 3.4, we demonstrate the effect of different spin recoil models on the halo mass$-$MBH mass relation. While a halo may still host an MBH seed at $z = 5$ when gravitational recoil is considered, multiple episodes of ejection and replenishment affects the mass of that seed. The incorporation of a recoil model can decrease the mean final MBH mass by as much

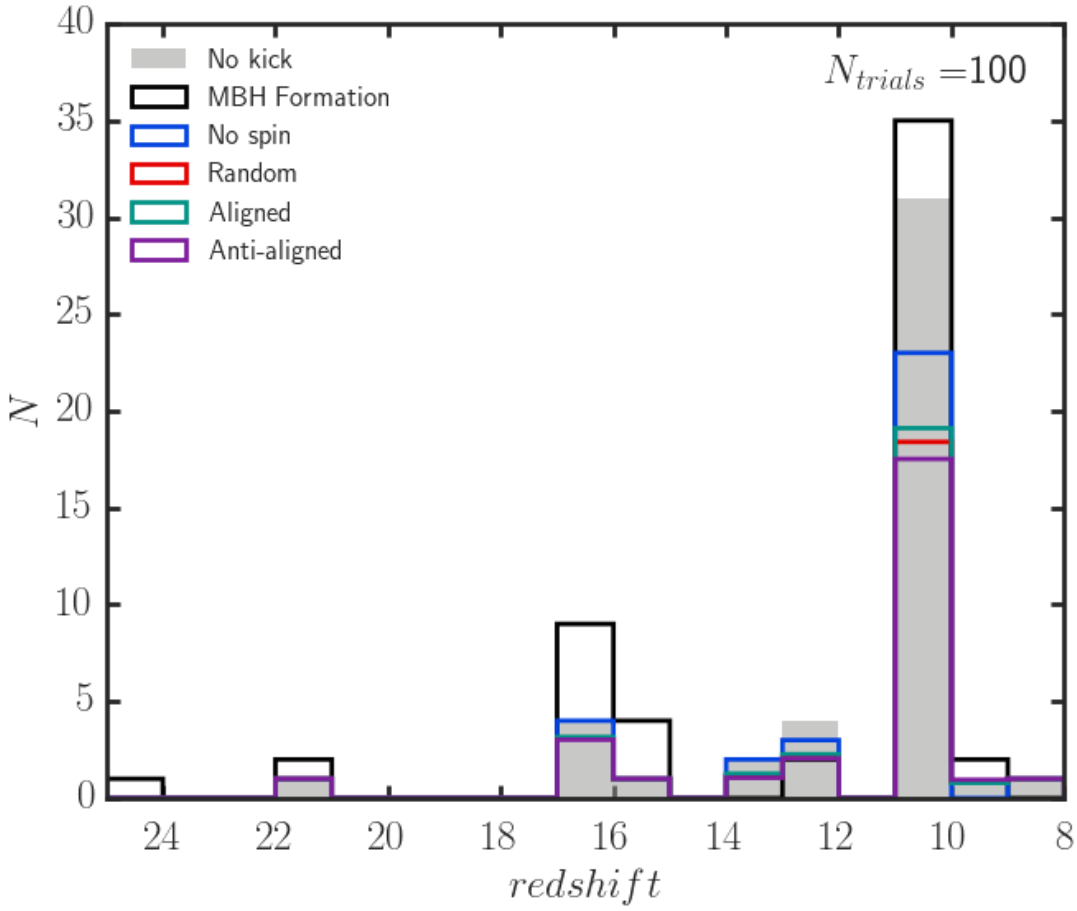

Figure 3.3: MBH-MBH MERGER HISTORY Comparison of the frequency of MBH mergers for different spin distributions to the MBH formation rate. The MBH formation history is shown in black, and the merger history for the original simulation with no recoil model is shown by the filled gray bars. While recoil models that result in larger kick velocities suppress the number of MBH-MBH mergers, all of the models show heightened merger rates during episodes of MBH formation. Merger histories computed for the random, aligned, and anti-aligned spin configurations are averaged over 100 trials.

as an order of magnitude. The random spin and anti-aligned spin models typically show the largest decrease in mean final MBH mass. Hosts that show no change in the mean final MBH mass do not experience any MBH-MBH mergers. The mean final MBH masses in these cases are equal to the initial MBH seed mass. Here we demonstrate two pathways for a halo in this simulation to to retain a central black hole with a mass resembling that of the original seed down to $z = 5$. In one scenario, a host halo may form only a single seed, and experience no events that feed this seed via either mergers with other black holes or accretion. Alternatively, a host may form multiple seeds at high redshift, but repeatedly eject the merged remnants from its shallow potential well.

Similarly, in Figure 3.5, we demonstrate the effect of different spin recoil models on the stellar mass−MBH mass relation. We multiply the stellar masses by 0.6 to convert simulated masses to observed masses as described in Munshi et al. (2013). For comparison, we over-plot the $z = 0$ $M_{\rm BH} - M_{\rm stellar}$ relations for local galaxies with stellar masses in the range $10^8 - 10^{12} M_{\odot}$ provided by Reines & Volonteri (2015). Gravitational recoil can be a significant source of scatter in these scaling relations, potentially up to an order of magnitude. This effect can skew $M_{\rm BH} - M_{\rm stellar}$ values below the expected relations, by indirectly increasing central star formation.

Mergers are plentiful in the assembly history of this Milky Way-type galaxy. Even if MBH mergers are electromagnetically dark, they are ideally suited for detection through gravitational waves. LISA is optimally designed to detect MBH mergers in the low-frequency regime, ranging from 10^4 to $10^7 \mathrm{M}_{\odot}$ in mass and out to redshifts larger than $z \sim 20$ (Amaro-Seoane et al., 2017). In Figure 3.6, we show the distribution of MBH merger masses and redshifts generated in this work against LISA S/N ratio contours in a 'waterfall' figure. Each black point marks a merger in our 'no spin' semi-analytic recoil model against the S/N contours that are a function of the redshift and combined total mass of the merging MBHs. These S/N values are approximate, as the rainbow contours are generated for 1:4 mass ratio mergers, but the most common mergers in these simulations have 1:1 and 1:2 mass ratios.

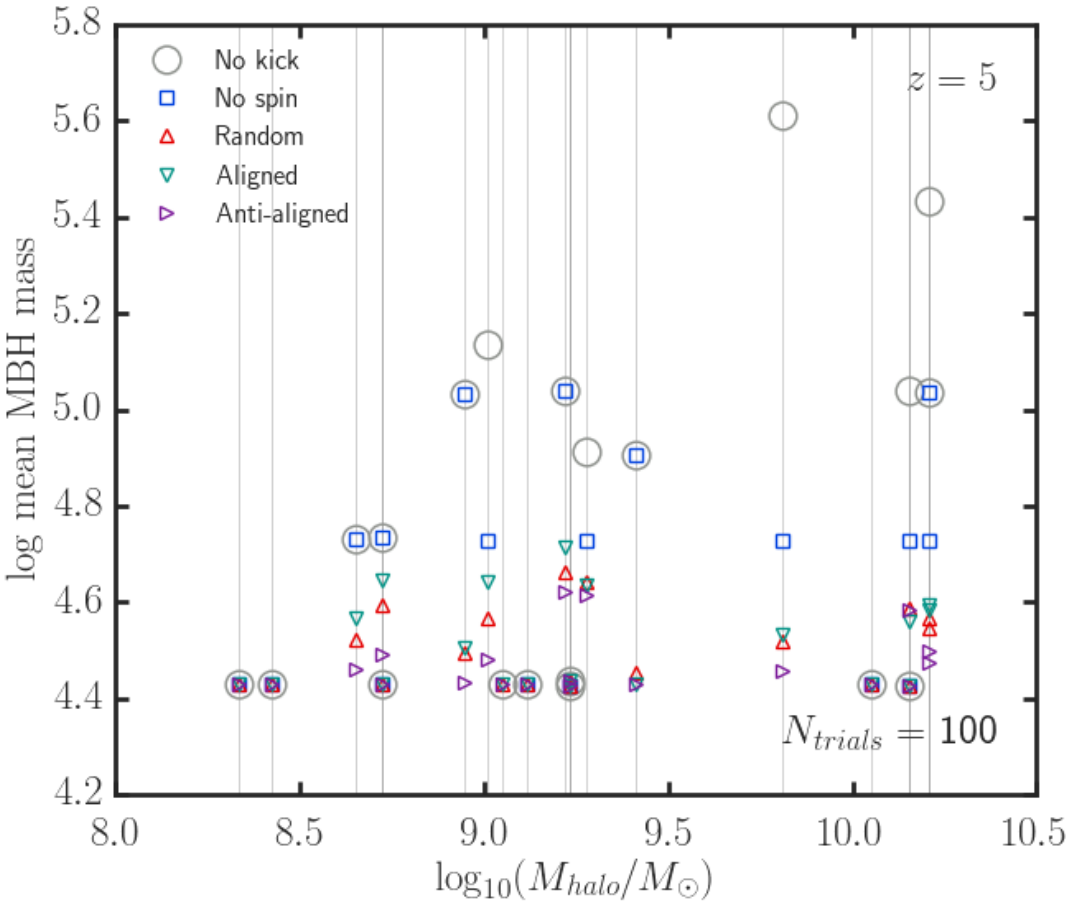

Figure 3.4: HALO MASS - BLACK HOLE MASS RELATION Each colored shape shows the mean final MBH masses in the different spin-recoil models. Grey vertical lines mark the mass of each host halo and serve to guide the eye. Vertical displacement between the fiducial 'no kick' mass and the final MBH masses associated with other models indicate that an MBH's assembly history was modified by at least one episode of merging, ejection, and refill. At $z = 5$, the incorporation of recoil velocity and different spin models decrease the average MBH mass. The random and anti-aligned spin configurations yield lower final average MBH masses. Black hole masses computed for the random, aligned, and anti-aligned spin configurations are averaged over 100 trials.

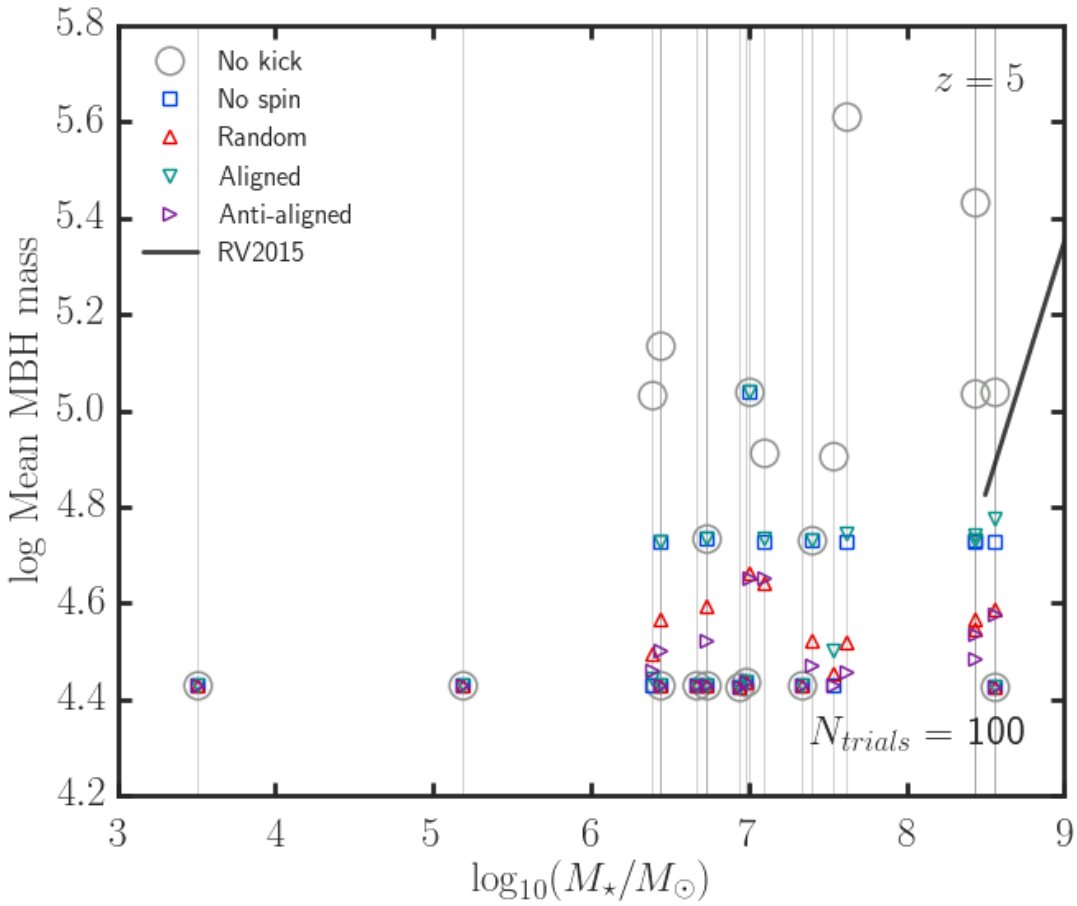

Figure 3.5: STELLAR MASS - BLACK HOLE MASS RELATION This figure is constructed similarly to Figure 3.4, but instead shows black hole mass as a function of stellar mass. The random and anti-aligned spin configurations yield lower final average MBH masses. Grey vertical lines mark the stellar mass of each host and serve to guide the eye. Black hole masses computed for the random, aligned, and anti-aligned spin configurations are averaged over 100 trials. For comparison, we include the $z = 0$ relation described by Reines & Volonteri (2015) for halos with stellar masses in the range $10^8 - 10^{12} M_\odot$.

These mergers occur throughout the epoch of MBH formation, and the cluster of events at $z \sim 11$ coincides with the peak of MBH formation. LISA detections of MBH-MBH mergers will constrain MBH formation scenarios, masses, and redshifts.

The next generation of space-based observatories will offer some of the first observational constraints of the formation and early growth of massive black hole seeds. The planned Lynx mission will have the sensitivity to detect objects at the low-luminosity and high-redshift ends of the quasar luminosity function. The James Webb Space Telescope (JWST) could potentially differentiate between massive black hole seed formation mechanisms (e.g., Natarajan et al., 2017). LISA will constrain the population of black holes with masses $10^4 - 10^7 M_\odot$, offering the first observational constraints of these electro-magnetically dark high-redshift objects. Assumptions about MBH merger fractions and recoil fractions, even physically motivated assumptions, will leave an imprint on predictions of the observable signatures of these objects. Predictions of the unresolved X-ray background, gravitational wave events, and the quasar luminosity function (especially the low-luminosity end) (e.g., Manti et al., 2017; Ricarte & Natarajan, 2018), are directly affected by the assumed merger and recoil fractions. Any work that attempts to disentangle the relationship between black hole formation and AGN observables must also address the physics of black hole mergers and gravitational recoil.

3.5 Summary

We studied the role of gravitational recoil in the mass assembly of massive black hole seeds using cosmological zoom-in simulations and a semi-analytic model for gravitational recoil velocities. Our results underline that gravitational wave recoil stifles the early growth of the seem MBHs, and alters the assembly pathways of MBHs and their host galaxies. In environments where multiple MBHs can form in bursts, gravitational recoil can prevent

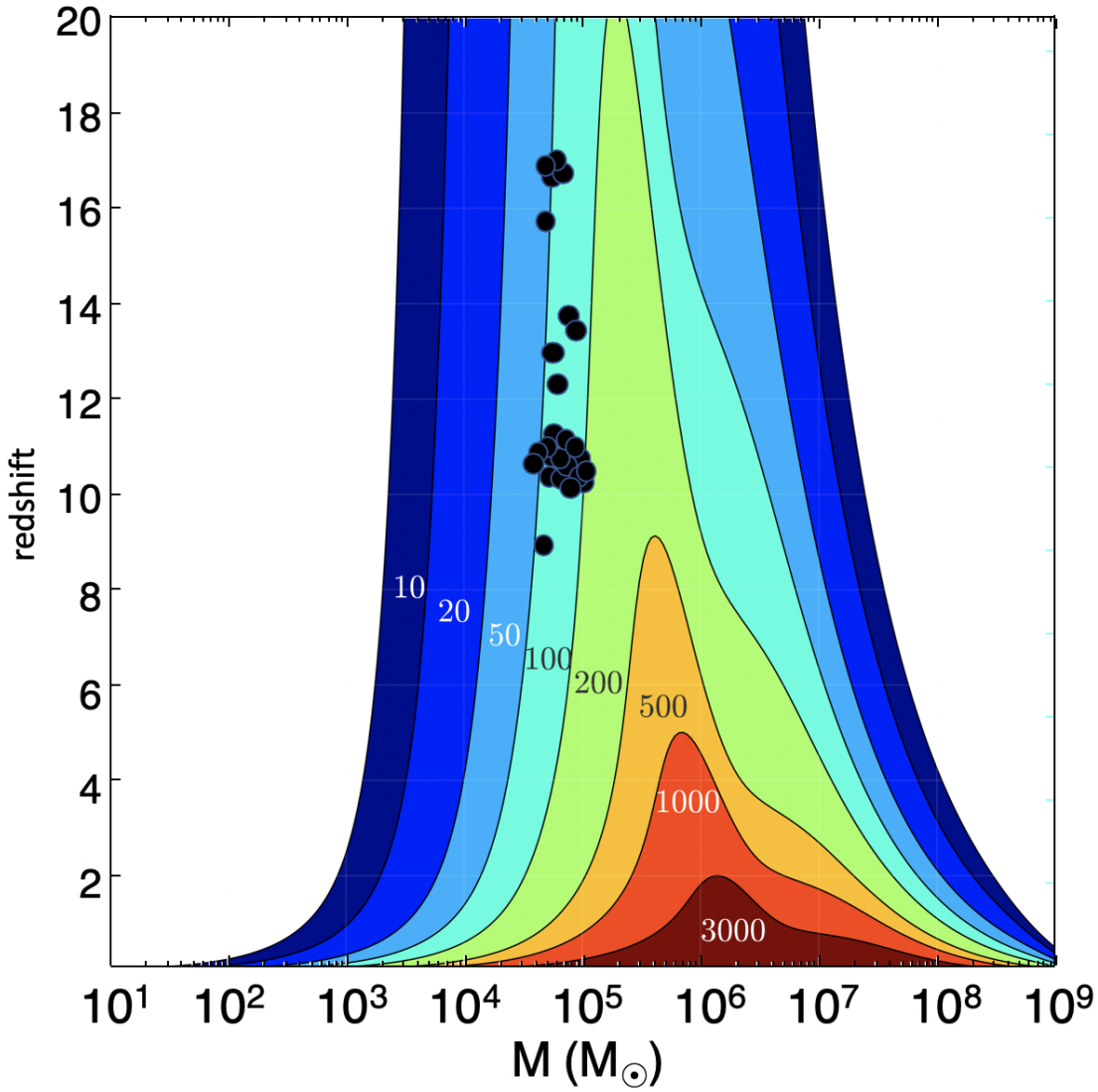

Figure 3.6: LISA SIGNAL Mergers are plentiful in the assembly history of this galaxy. The black points in this figure represent the MBH mergers that occur during the assembly of this Milky Way-type halo. The colored contours represent the S/N ratios with which LISA would detect mergers with a mass ratio of 0.25. This sample of synthetic LISA source signals is drawn from the 'no spin' recoil model. The large cluster of sources in the redshift range $z \sim 10-12$ represents the spike in MBH-MBH mergers that results from a simultaneous spike in MBH formation. The merger that occurs at $z = 22$ is not shown.

the rapid growth of black holes by mergers, as these mergers typically eject the remnant. However, these same bursts of black hole formation also allow an empty halo to be refilled with new MBH seeds. The restocking of a proto-galactic host is reflected in the statistical agreement of MBH occupation fractions associated with different recoil models. The masses of the final MBHs, however, may be significantly reduced, and more closely resemble the initial seed mass. The differences in final MBH masses may inject scatter into observable scaling relations and provide tension with these relations.

MBH mergers are likely an important component of MBH-galaxy co-evolution. Even if an MBH-MBH merger is not ejected from its host, the recoil velocity may still be large enough to force the MBH to wander the outskirts of the host galaxy or dark matter halo (Holley-Bockelmann et al., 2008; Bellovary et al., 2010). As the MBH wends its way toward the center via dynamical friction, accretion is likely minimal (van Wassenhove et al., 2010), but if it encounters a pocket of gas with low relative velocity (e.g., at apocenter), it can outshine its host as an off-center AGN (Blecha et al., 2016; Comerford et al., 2015) as seen in NGC 3115 (Menezes et al., 2014). This trajectory through the host allows the merged MBH to accrete, modifying the object's mass and spin, and possibly allow it to avoid capture into another binary system (Guedes et al., 2011).

MBH-MBH mergers are ideal LISA candidates, particularly mergers of MBH seeds at redshifts $10-20$ such as those discussed in this work. LISA observations of gravitational wave emissions from these mergers will likely provide some of the first insights into the lives of the first black holes. While gas accretion erases clues about MBH formation long before these black holes are electromagnetically observable, gravitational waves from pre-reionization merger events will provide a more direct probe of the seed black hole population. These observations will characterize the number density, masses, and redshifts of black hole mergers, and have the potential to help constrain seed formation scenarios.

In future work, it will be important to study this phenomenon with a suite of galaxies at different masses and assembly histories. If ejections of merged binary black holes are

common, gravitational recoil may be a serious impediment to the rapid accumulation of black hole mass necessary to create both high-z quasars and low-z black hole-host scaling relations.

Chapter 4

Summary and future work

4.1 Future Work

Here, I discuss a few possibilities for future projects that are made possible by the work in this Thesis. First, I present two complementary methods for extending this work in an effort to build a statistical picture of direct collapse black hole formation in a variety of halos. Second, I discuss the need to the calculate gravitational wave signals from the black hole mergers presented in Chapter 3. Finally, I discuss the opportunity to study the orbits, spin evolution, and accretion of merged black holes that wander throughout their host halos.

4.1.1 Building a statistical description of direct collapse: modeling a diverse suite of halos

In Chapter 2 we describe a study of Lyman-Werner driven direct collapse in a Milky Way analog. Such a study is well-motivated in part because supermassive black holes in galaxies like the Milky Way are thought to be some of the most ubiquitous types of SMBH in the Universe, but are much less commonly studied that their more massive counterparts. One limitation of this work, however, is that it does not lend itself to a statistical description of the direct collapse process. This work is effectively a case study, in which we study the phenomenon of Lyman-Werner driven direct collapse as a part of the assembly of a single $z = 0$ galaxy. A zoom-in simulation of a single Milky Way-mass galaxy with an active interaction history clearly does not sample an unbiased portion of the Universe. However, GASOLINE initial conditions exist for a wide variety of galaxy masses and assembly histories, ranging from dwarf galaxies to massive ellipticals. A suite of simulations of different galaxies would build a broad picture of massive black hole seed

formation as a function of halo mass, environment, and merger history.

4.1.2 Building a statistical description of direct collapse: integrating this work into a semi-analytic model

A statistical description of massive black hole seed formation will make global predictions about black hole demographics, high-redshift X-ray background radiation, merger rates, and gravitational wave signal possible. A semi-analytic model informed by predictions from the hydrodynamical models presented in this Thesis could provide statistical information about massive black hole formation and high-redshift growth and inform how the processes affect black hole demographics. Semi-analytic models also provide a framework for easily incorporating additional black hole physics, as we demonstrated in Chapter 3. The results of such a semi-analytic model will allow us to map the physics of direct collapse to observables such as the $M - \sigma$ relation.

4.1.3 Gravitational wave signal from MBH-MBH mergers

Merging massive black holes are likely the loudest sources of gravitational waves in the Universe. A natural extension of the work in this Thesis is to calculate the gravitational wave strain from the black hole mergers presented in Chapter 3. The mergers that we predict in this Thesis occur well before re-ionization, and while they would not be observable with electromagnetic detectors, they are prime targets for gravitational wave detection with *LISA*. Gravitational wave detections of merging binary black holes with *LISA* will yield measurements of black hole masses and spins accurate to a few percent, delivering insight into seed masses, accretion histories, and co-evolution with host galaxies.

4.1.4 Sloshing black holes

What happens to the black holes that neither escape nor remain fixed at the center of their host galaxies after experiencing a merger? These black holes will wander, or 'slosh' through the host halo before eventually settling back towards the center of the host. Black hole mergers caused by hierarchical galaxy formation can wander as far as $\sim 10-100$ kpc from the center of the host halo (Bellovary et al., 2010; Tremmel et al., 2018), and may oscillate throughout the host galaxy for up to a Gyr (Blecha & Loeb, 2008). Future work building on the results of Chapter 3 could model the orbits, spin evolution, and accretion rates of the population of black holes that slosh throughout the inner few kpc of the halo. Semi-analytic modeling of the orbit and spin evolution of a merged black hole in a fixed galactic potential would provide more accurate merger times for subsequent black hole mergers in a halo.

4.2 Summary

This Thesis presents the first work to self-consistently model the formation of direct collapse black holes in the presence of spatially and temporally varying Lyman-Werner radiation in cosmological simulations. We constructed a probabilistic model direct collapse black hole formation in GASOLINE that evaluates gas particles for black hole candidacy based on local density, metallicity, and Lyman-Werner radiation. We applied this model to a set of three zoom-in simulations of the assembly of a Milky Way-type galaxy that bracketed the range of predicted values of $J_{\rm crit}$: $30-10^3 J_{21}$. From these simulations, we demonstrate the possibility that direct collapse can occur in halos with recent star formation,

and that multiple black hole seeds can form in a single halo. This is a shift away from the canonical theory that only a single direct collapse black hole can form in a halo, which must be pristine, with no history of star formation. This work may indicate that direct collapse black hole seeds are less rare than once expected.

If multiple seeds can form nearly simultaneously in a single halo, these seeds have the potential to grow quickly through MBH-MBH mergers. We applied a semi-analytic model for spin-dependent recoil velocity to the black hole merger tree from our most conservative $J_{\rm crit}$ model: $J_{\rm crit} = 10^3 J_{21}$. The black hole mergers that we predict in this work are caused by bursts of massive black hole seed formation. At the high redshifts that provide environments favorable for direct collapse, the host halos are still quite small, and merged black holes with large recoil velocities may escape their hosts. We find that gravitational recoil restricts MBH-MBH mergers as a pathway for the rapid growth of MBH seeds. When several MBH seeds can form sequentially in a single halo, the merged black typically escapes its host after $1-3$ mergers. After an ejection, subsequent epochs of black hole formation can replace the ejected black hole with a new seed. This cycle of black hole seed formation, mergers, and ejections may repeat, finally ending with the end of black hole formation, leaving a host halo with either no central black hole or one with a mass equal to $\sim$ a few seed masses. We find that this cycle of black hole formation, mergers, and ejections leaves a trace in the form of a final $z = 5$ MBH mass close to the original seed mass.

BIBLIOGRAPHY

Abbott, B. P., Abbott, R., Abbott, T. D., et al. 2016, Phys. Rev. Lett., 116, 061102

Abbott, B. P., Abbott, R., Abbott, T. D., et al. 2016, Phys. Rev. Lett., 116, 061102

Abel, T., Bryan, G. L., & Norman, M. L. 2002, Science, 295, 93

Agarwal, B., Dalla Vecchia, C., Johnson, J. L., Khochfar, S., & Paardekooper, J.-P. 2014, MNRAS, 443, 648

Agarwal, B., Davis, A. J., Khochfar, S., Natarajan, P., & Dunlop, J. S. 2013, MNRAS, 432, 3438

Agarwal, B., Smith, B., Glover, S., Natarajan, P., & Khochfar, S. 2016, MNRAS, 459, 4209

Agertz, O., Moore, B., Stadel, J., et al. 2007, MNRAS, 380, 963

Ahn, K., Shapiro, P. R., Iliev, I. T., Mellema, G., & Pen, U.-L. 2009, ApJ, 695, 1430

Alexander, T., & Natarajan, P. 2014, Science, 345, 1330

Alvarez, M. A., Wise, J. H., & Abel, T. 2009, ApJ, 701, L133

Amaro-Seoane, P., Audley, H., Babak, S., et al. 2017, ArXiv e-prints, arXiv:1702.00786

Antonini, F., Barausse, E., & Silk, J. 2015, ApJ, 812, 72

Araya Salvo, C., Mathur, S., Ghosh, H., Fiore, F., & Ferrarese, L. 2012, ApJ, 757, 179

Aykutalp, A., Wise, J. H., Spaans, M., & Meijerink, R. 2014, ApJ, 797, 139

Bañados, E., Venemans, B. P., Decarli, R., et al. 2016, ApJS, 227, 11

Bañados, E., Venemans, B. P., Mazzucchelli, C., et al. 2018, Nature, 553, 473

Baker, J. G., Boggs, W. D., Centrella, J., et al. 2008, ApJ, 682, L29

Baldassare, V. F., Geha, M., & Greene, J. 2018, ApJ, 868, 152

Barausse, E. 2012, MNRAS, 423, 2533

Barkana, R., & Loeb, A. 2001, Phys. Rep., 349, 125

Begelman, M. C. 2010, MNRAS, 402, 673

Begelman, M. C., & Rees, M. J. 1978, MNRAS, 185, 847

Begelman, M. C., Rossi, E. M., & Armitage, P. J. 2008, MNRAS, 387, 1649

Begelman, M. C., & Shlosman, I. 2009, ApJ, 702, L5

Begelman, M. C., Volonteri, M., & Rees, M. J. 2006, MNRAS, 370, 289

Bekenstein, J. D. 1973, ApJ, 183, 657

Bellovary, J., Volonteri, M., Governato, F., et al. 2011, ApJ, 742, 13

Bellovary, J. M., Governato, F., Quinn, T. R., et al. 2010, ApJ, 721, L148

Bernardi, M., Sheth, R. K., Tundo, E., & Hyde, J. B. 2007, ApJ, 660, 267

Blecha, L., Cox, T. J., Loeb, A., & Hernquist, L. 2011, MNRAS, 412, 2154

Blecha, L., & Loeb, A. 2008, MNRAS, 390, 1311

Blecha, L., Sijacki, D., Kelley, L. Z., et al. 2016, MNRAS, 456, 961

Bogdanović, T., Reynolds, C. S., & Miller, M. C. 2007, ApJ, 661, L147

Bonoli, S., Mayer, L., & Callegari, S. 2014, MNRAS, 437, 1576

Booth, C. M., & Schaye, J. 2009, MNRAS, 398, 53

Bragg, A. E., Greenhill, L. J., Moran, J. M., & Henkel, C. 2000, ApJ, 535, 73

Bromm, V., Coppi, P. S., & Larson, R. B. 2002, ApJ, 564, 23

Bromm, V., & Loeb, A. 2003, ApJ, 596, 34

Brooks, A. M., Governato, F., Booth, C. M., et al. 2007, ApJ, 655, L17

Brooks, A. M., Solomon, A. R., Governato, F., et al. 2011, ApJ, 728, 51

Campanelli, M., Lousto, C., Zlochower, Y., & Merritt, D. 2007a, ApJ, 659, L5

Campanelli, M., Lousto, C. O., Zlochower, Y., & Merritt, D. 2007b, Physical Review Letters, 98, 231102

Capelo, P. R., Volonteri, M., Dotti, M., et al. 2015, MNRAS, 447, 2123

Cazaux, S., & Spaans, M. 2009, A&A, 496, 365

Choi, J.-H., Shlosman, I., & Begelman, M. C. 2013, ApJ, 774, 149

—. 2015, MNRAS, 450, 4411

Chon, S., Hirano, S., Hosokawa, T., & Yoshida, N. 2016, ApJ, 832, 134

Christensen, C., Quinn, T., Governato, F., et al. 2012, MNRAS, 425, 3058

Christensen, C. R., Brooks, A. M., Fisher, D. B., et al. 2014, MNRAS, 440, L51

Christensen, C. R., Davé, R., Governato, F., et al. 2016, ApJ, 824, 57

Christensen, C. R., Quinn, T., Stinson, G., Bellovary, J., & Wadsley, J. 2010, ApJ, 717, 121

Clark, P. C., Glover, S. C. O., & Klessen, R. S. 2008, ApJ, 672, 757

Colpi, M., Holley-Bockelmann, K., Bogdanović, T., et al. 2019, in BAAS, Vol. 51, 432

Comerford, J. M., Pooley, D., Barrows, R. S., et al. 2015, ApJ, 806, 219

Davies, M. B., Miller, M. C., & Bellovary, J. M. 2011, ApJ, 740, L42

De Rosa, G., Venemans, B. P., Decarli, R., et al. 2014, ApJ, 790, 145

Debuhr, J., Quataert, E., & Ma, C.-P. 2011, MNRAS, 412, 1341

Devecchi, B., Rasia, E., Dotti, M., Volonteri, M., & Colpi, M. 2009, MNRAS, 394, 633

Devecchi, B., & Volonteri, M. 2009, ApJ, 694, 302

Di Matteo, T., Colberg, J., Springel, V., Hernquist, L., & Sijacki, D. 2008, ApJ, 676, 33

Di Matteo, T., Springel, V., & Hernquist, L. 2005, Nature, 433, 604

Dijkstra, M., Ferrara, A., & Mesinger, A. 2014, MNRAS, 442, 2036

Dijkstra, M., Haiman, Z., Mesinger, A., & Wyithe, J. S. B. 2008, MNRAS, 391, 1961

Dotti, M., Volonteri, M., Perego, A., et al. 2010, MNRAS, 402, 682

Dubois, Y., Devriendt, J., Slyz, A., & Teyssier, R. 2012a, MNRAS, 420, 2662

Dubois, Y., Peirani, S., Pichon, C., et al. 2016, MNRAS, 463, 3948

Dubois, Y., Pichon, C., Haehnelt, M., et al. 2012b, MNRAS, 423, 3616

Dunn, G., Bellovary, J., Holley-Bockelmann, K., Christensen, C., & Quinn, T. 2018, ApJ, 861, 39

Eisenstein, D. J., & Loeb, A. 1995, ApJ, 443, 11

Fabian, A. C. 2012, ARA&A, 50, 455

Fan, X., Strauss, M. A., Schneider, D. P., et al. 2003, AJ, 125, 1649

Ferrarese, L., & Merritt, D. 2000, ApJ, 539, L9

Ferrarese, L., Côté, P., Dalla Bontà, E., et al. 2006, ApJ, 644, L21

Ferré-Mateu, A., Mezcua, M., Trujillo, I., Balcells, M., & van den Bosch, R. C. E. 2015, ApJ, 808, 79

Gebhardt, K., Bender, R., Bower, G., et al. 2000, ApJ, 539, L13

Gerosa, D., & Moore, C. J. 2016, Physical Review Letters, 117, 011101

Gerosa, D., & Sesana, A. 2015, MNRAS, 446, 38

Ghez, A. M., Salim, S., Hornstein, S. D., et al. 2005, ApJ, 620, 744

Gill, S. P. D., Knebe, A., & Gibson, B. K. 2004, MNRAS, 351, 399

Glover, S. C. O. 2011, in IAU Symposium, Vol. 280, The Molecular Universe, ed. J. Cernicharo & R. Bachiller, 313–324

Glover, S. C. O. 2015a, MNRAS, 451, 2082

—. 2015b, MNRAS, 453, 2901

—. 2016, ArXiv e-prints, arXiv:1610.05679

González, J. A., Hannam, M., Sperhake, U., Brügmann, B., & Husa, S. 2007, Physical Review Letters, 98, 231101

Goulding, A. D., Greene, J. E., Bezanson, R., et al. 2018, PASJ, 70, S37

Governato, F., Brook, C. B., Brooks, A. M., et al. 2009, MNRAS, 398, 312

Governato, F., Brook, C., Mayer, L., et al. 2010, Nature, 463, 203

Governato, F., Weisz, D., Pontzen, A., et al. 2015, MNRAS, 448, 792

Graham, A. W. 2008, ApJ, 680, 143

—. 2012, MNRAS, 422, 1586

Graham, A. W., Onken, C. A., Athanassoula, E., & Combes, F. 2011, MNRAS, 412, 2211

Greenhill, L. J., Jiang, D. R., Moran, J. M., et al. 1995, ApJ, 440, 619

Grier, C. J., Shen, Y., Horne, K., et al. 2019, arXiv e-prints, arXiv:1904.03199

Guedes, J., Madau, P., Mayer, L., & Callegari, S. 2011, ApJ, 729, 125

Gültekin, K., Richstone, D. O., Gebhardt, K., et al. 2009, ApJ, 698, 198

Haardt, F., & Madau, P. 1996, ApJ, 461, 20

Habouzit, M., Volonteri, M., Latif, M., Dubois, Y., & Peirani, S. 2016, MNRAS, 463, 529

Haiman, Z. 2006, New Astronomy Reviews, 50, 672

Haiman, Z., Abel, T., & Rees, M. J. 2000, ApJ, 534, 11

Haiman, Z., & Loeb, A. 2001, ApJ, 552, 459

Haiman, Z., Rees, M. J., & Loeb, A. 1996, ApJ, 467, 522

Häring, N., & Rix, H.-W. 2004, ApJ, 604, L89

Harris, G. L. H., & Harris, W. E. 2011, MNRAS, 410, 2347

Harris, G. L. H., Poole, G. B., & Harris, W. E. 2014, MNRAS, 438, 2117

Harrison, C. M. 2017, Nature Astronomy, 1, 0165

Hartwig, T., Bromm, V., Klessen, R. S., & Glover, S. C. O. 2015, MNRAS, 447, 3892

Hartwig, T., Volonteri, M., & Dashyan, G. 2018, MNRAS, 476, 2288

Heckman, T. M., & Best, P. N. 2014, ARA&A, 52, 589

Heger, A., & Woosley, S. E. 2002, ApJ, 567, 532

Herrmann, F., Hinder, I., Shoemaker, D., Laguna, P., & Matzner, R. A. 2007, ApJ, 661, 430

Hirano, S., Hosokawa, T., Yoshida, N., & Kuiper, R. 2017, Science, 357, 1375

Holley-Bockelmann, K., Gültekin, K., Shoemaker, D., & Yunes, N. 2008, ApJ, 686, 829

Holley-Bockelmann, K., Micic, M., Sigurdsson, S., & Rubbo, L. J. 2010, ApJ, 713, 1016

Holley-Bockelmann, K., Wise, J. H., & Sinha, M. 2012, ApJ, 761, L8

Hosokawa, T., Omukai, K., Yoshida, N., & Yorke, H. W. 2011, Science, 334, 1250

Hosokawa, T., Yorke, H. W., Inayoshi, K., Omukai, K., & Yoshida, N. 2013, ApJ, 778, 178

Johnson, J. L., & Bromm, V. 2007, MNRAS, 374, 1557

Johnson, J. L., Whalen, D. J., Agarwal, B., Paardekooper, J.-P., & Khochfar, S. 2014, MNRAS, 445, 686

Kaspi, S., Smith, P. S., Netzer, H., et al. 2000, ApJ, 533, 631

Katz, H., Sijacki, D., & Haehnelt, M. G. 2015, MNRAS, 451, 2352

Katz, N., & White, S. D. M. 1993, ApJ, 412, 455

Kelley, L. Z., Blecha, L., & Hernquist, L. 2017, MNRAS, 464, 3131

Kim, M., Ho, L. C., Peng, C. Y., et al. 2008, ApJ, 687, 767

Knollmann, S. R., & Knebe, A. 2009, ApJS, 182, 608

Kormendy, J., & Ho, L. C. 2013, ARA&A, 51, 511

Kormendy, J., & Richstone, D. 1995, ARA&A, 33, 581

Koss, M. J., Blecha, L., Bernhard, P., et al. 2018, Nature, 563, 214

Koushiappas, S. M., Bullock, J. S., & Dekel, A. 2004, MNRAS, 354, 292

Kroupa, P. 2001, MNRAS, 322, 231

Kroupa, P., Tout, C. A., & Gilmore, G. 1993, MNRAS, 262, 545

Kurk, J. D., Walter, F., Fan, X., et al. 2007, ApJ, 669, 32

Latif, M. A., Bovino, S., Grassi, T., Schleicher, D. R. G., & Spaans, M. 2015, MNRAS, 446, 3163

Latif, M. A., Bovino, S., Van Borm, C., et al. 2014, MNRAS, 443, 1979

Latif, M. A., Omukai, K., Habouzit, M., Schleicher, D. R. G., & Volonteri, M. 2016, ApJ, 823, 40

Latif, M. A., Schleicher, D. R. G., Schmidt, W., & Niemeyer, J. 2013a, MNRAS, 433, 1607

—. 2013b, MNRAS, 430, 588

Latif, M. A., Schleicher, D. R. G., Schmidt, W., & Niemeyer, J. C. 2013c, MNRAS, 436, 2989

Leitherer, C., Schaerer, D., Goldader, J. D., et al. 1999, ApJS, 123, 3

Libeskind, N. I., Cole, S., Frenk, C. S., & Helly, J. C. 2006, MNRAS, 368, 1381

Lippai, Z., Frei, Z., & Haiman, Z. 2009, ApJ, 701, 360

Lodato, G., & Gerosa, D. 2013, MNRAS, 429, L30

Lodato, G., & Natarajan, P. 2006, MNRAS, 371, 1813

—. 2007, MNRAS, 377, L64

Loeb, A., & Rasio, F. A. 1994, ApJ, 432, 52

Lousto, C. O., & Zlochower, Y. 2011, Phys. Rev. Lett., 107, 231102

Madau, P., & Rees, M. J. 2001, ApJ, 551, L27

Magorrian, J., Tremaine, S., Richstone, D., et al. 1998, AJ, 115, 2285

Maiolino, R., Russell, H. R., Fabian, A. C., et al. 2017, Nature, 544, 202

Manti, S., Gallerani, S., Ferrara, A., Greig, B., & Feruglio, C. 2017, MNRAS, 466, 1160

Mapelli, M. 2016, MNRAS, 459, 3432

Marleau, F. R., Clancy, D., Habas, R., & Bianconi, M. 2017, A&A, 602, A28

McBride, J., Fakhouri, O., & Ma, C.-P. 2009, MNRAS, 398, 1858

McConnell, N. J., & Ma, C.-P. 2013, ApJ, 764, 184

McConnell, N. J., Ma, C.-P., Murphy, J. D., et al. 2012, ApJ, 756, 179

Menezes, R. B., Steiner, J. E., & Ricci, T. V. 2014, ApJ, 796, L13

Menou, K., Haiman, Z., & Narayanan, V. K. 2001, ApJ, 558, 535

Merritt, D., & Ferrarese, L. 2001, MNRAS, 320, L30

Merritt, D., & Milosavljević, M. 2005, Living Reviews in Relativity, 8, astro-ph/0410364

Merritt, D., Milosavljević, M., Favata, M., Hughes, S. A., & Holz, D. E. 2004, ApJ, 607, L9

Meyer, L., Ghez, A. M., Schödel, R., et al. 2012, Science, 338, 84

Mezcua, M., Civano, F., Marchesi, S., et al. 2018, MNRAS, 478, 2576

Micic, M., Abel, T., & Sigurdsson, S. 2006, MNRAS, 372, 1540

Micic, M., Holley-Bockelmann, K., & Sigurdsson, S. 2008, ArXiv e-prints, arXiv:0805.3154

—. 2011, MNRAS, 414, 1127

Micic, M., Holley-Bockelmann, K., Sigurdsson, S., & Abel, T. 2007, MNRAS, 380, 1533

Miller, B. P., Gallo, E., Greene, J. E., et al. 2015, ApJ, 799, 98

Miyoshi, M., Moran, J., Herrnstein, J., et al. 1995, Nature, 373, 127

Monaghan, J. J. 1992, ARA&A, 30, 543

Mortlock, D. J., Warren, S. J., Venemans, B. P., et al. 2011, Nature, 474, 616

Munshi, F., Christensen, C., Quinn, T. R., et al. 2014, ApJ, 781, L14

Munshi, F., Governato, F., Brooks, A. M., et al. 2013, ApJ, 766, 56

Natarajan, P., Pacucci, F., Ferrara, A., et al. 2017, ApJ, 838, 117

Oh, S. P., & Haiman, Z. 2002, ApJ, 569, 558

Okamoto, T., Nemmen, R. S., & Bower, R. G. 2008, MNRAS, 385, 161

Omukai, K., Schneider, R., & Haiman, Z. 2008, ApJ, 686, 801

Peirani, S., Dubois, Y., Volonteri, M., et al. 2017, MNRAS, 472, 2153

Pezzulli, E., Valiante, R., & Schneider, R. 2016, MNRAS, 458, 3047

Pontzen, A., Roškar, R., Stinson, G., & Woods, R. 2013, pynbody: N-Body/SPH analysis for python, Astrophysics Source Code Library, ascl:1305.002

Power, C., Navarro, J. F., Jenkins, A., et al. 2003, MNRAS, 338, 14

Prieto, J., Jimenez, R., & Haiman, Z. 2013, MNRAS, 436, 2301

Regan, J. A., & Downes, T. P. 2018, MNRAS, 475, 4636

Regan, J. A., Johansson, P. H., & Wise, J. H. 2014, ApJ, 795, 137

—. 2016, MNRAS, 461, 111

Regan, J. A., Visbal, E., Wise, J. H., et al. 2017, Nature Astronomy, 1, 0075

Reines, A. E., Sivakoff, G. R., Johnson, K. E., & Brogan, C. L. 2011, Nature, 470, 66

Reines, A. E., & Volonteri, M. 2015, ApJ, 813, 82

Ricarte, A., & Natarajan, P. 2018, MNRAS, 481, 3278

Ritchie, B. W., & Thomas, P. A. 2001, MNRAS, 323, 743

Sadoun, R., & Colin, J. 2012, MNRAS, 426, L51

Saglia, R. P., Opitsch, M., Erwin, P., et al. 2016, ApJ, 818, 47

Sakurai, Y., Yoshida, N., Fujii, M. S., & Hirano, S. 2017, MNRAS, 472, 1677

Satyapal, S., Böker, T., Mcalpine, W., et al. 2009, ApJ, 704, 439

Schauer, A. T. P., Regan, J., Glover, S. C. O., & Klessen, R. S. 2017a, MNRAS, 471, 4878

Schauer, A. T. P., Agarwal, B., Glover, S. C. O., et al. 2017b, MNRAS, 467, 2288

Schleicher, D. R. G., Palla, F., Ferrara, A., Galli, D., & Latif, M. 2013, A&A, 558, A59

Schnittman, J. D., & Buonanno, A. 2007, ApJ, 662, L63

Scoccimarro, R. 1998, MNRAS, 299, 1097

Secrest, N. J., Satyapal, S., Gliozzi, M., et al. 2015, ApJ, 798, 38

Shang, C., Bryan, G. L., & Haiman, Z. 2010, MNRAS, 402, 1249

Shen, S., Wadsley, J., & Stinson, G. 2010, MNRAS, 407, 1581

Shlosman, I., Frank, J., & Begelman, M. C. 1989, Nature, 338, 45

Sijacki, D., Springel, V., Di Matteo, T., & Hernquist, L. 2007, MNRAS, 380, 877

Sijacki, D., Springel, V., & Haehnelt, M. G. 2009, MNRAS, 400, 100

Simmons, B. D., Lintott, C., Schawinski, K., et al. 2013, MNRAS, 429, 2199

Simmons, B. D., Lintott, C., Willett, K. W., et al. 2017, MNRAS, 464, 4420

Smith, B. D., Regan, J. A., Downes, T. P., et al. 2018, MNRAS, 480, 3762

Spaans, M., & Silk, J. 2006, ApJ, 652, 902

Spergel, D. N., Bean, R., Doré, O., et al. 2007, ApJS, 170, 377

Stacy, A., Bromm, V., & Lee, A. T. 2016, MNRAS, 462, 1307

Stacy, A., Greif, T. H., & Bromm, V. 2010, MNRAS, 403, 45

Stadel, J. G. 2001, PhD thesis, UNIVERSITY OF WASHINGTON

Stinson, G., Seth, A., Katz, N., et al. 2006, MNRAS, 373, 1074

Suazo, M., Prieto, J., Escala, A., & Schleicher, D. 2019, arXiv e-prints, arXiv:1903.03637

Subramanian, S., Ramya, S., Das, M., et al. 2016, MNRAS, 455, 3148

Sugimura, K., Omukai, K., & Inoue, A. K. 2014, MNRAS, 445, 544

Tanaka, T., & Haiman, Z. 2009, ApJ, 696, 1798

Tanaka, T., Perna, R., & Haiman, Z. 2012, MNRAS, 425, 2974

Tanaka, T. L., & Li, M. 2014, MNRAS, 439, 1092

Tang, J.-J., Goto, T., Ohyama, Y., et al. 2019, MNRAS, 484, 2575

Treister, E., Schawinski, K., Volonteri, M., Natarajan, P., & Gawiser, E. 2011, Nature, 474, 356

Tremaine, S., Gebhardt, K., Bender, R., et al. 2002, ApJ, 574, 740

Tremmel, M., Governato, F., Volonteri, M., Pontzen, A., & Quinn, T. R. 2018, ApJ, 857, L22

Tremmel, M., Karcher, M., Governato, F., et al. 2017, MNRAS, 470, 1121

Umeda, H., Hosokawa, T., Omukai, K., & Yoshida, N. 2016, ApJ, 830, L34

van Wassenhove, S., Volonteri, M., Walker, M. G., & Gair, J. R. 2010, MNRAS, 408, 1139

Visbal, E., Bryan, G. L., & Haiman, Z. 2017, MNRAS, 469, 1456

Visbal, E., Haiman, Z., & Bryan, G. L. 2014a, MNRAS, 442, L100

—. 2014b, MNRAS, 445, 1056

Volonteri, M. 2007, ApJ, 663, L5

—. 2010, A&A Rev., 18, 279

Volonteri, M., & Bellovary, J. 2012, Reports on Progress in Physics, 75, 124901

Volonteri, M., Haardt, F., & Madau, P. 2003, ApJ, 582, 559

Volonteri, M., Lodato, G., & Natarajan, P. 2008, MNRAS, 383, 1079

Volonteri, M., & Natarajan, P. 2009, MNRAS, 400, 1911

Wadsley, J. W., Keller, B. W., & Quinn, T. R. 2017, MNRAS, 471, 2357

Wadsley, J. W., Stadel, J., & Quinn, T. 2004, Nature, 9, 137

Wise, J. H., Regan, J. A., O'Shea, B. W., et al. 2019, Nature, 566, 85

Wolcott-Green, J., Haiman, Z., & Bryan, G. L. 2011, MNRAS, 418, 838

—. 2017, MNRAS, 469, 3329

Woo, J.-H., Schulze, A., Park, D., et al. 2013, ApJ, 772, 49

Wyithe, J. S. B., & Loeb, A. 2003, ApJ, 595, 614

Xu, H., Wise, J. H., & Norman, M. L. 2013, ApJ, 773, 83

Yajima, H., & Khochfar, S. 2016, MNRAS, 457, 2423

Yoshida, N., Abel, T., Hernquist, L., & Sugiyama, N. 2003, ApJ, 592, 645

Yue, B., Ferrara, A., Pacucci, F., & Omukai, K. 2017, ApJ, 838, 111

Yue, B., Ferrara, A., Salvaterra, R., Xu, Y., & Chen, X. 2014, MNRAS, 440, 1263

Zel'dovich, Y. B. 1970, A&A, 5, 84

Zhu, Q., Li, Y., & Sherman, S. 2012, arXiv e-prints, arXiv:1211.0013

Zolotov, A., Brooks, A. M., Willman, B., et al. 2012, ApJ, 761, 71

Appendix A

Simulating direct collapse black hole formation

A.1 Preventing spurious overproduction of black holes

In GASOLINE, high resolution simulations executed with molecular hydrogen cooling and Lyman-Werner radiation driven black hole formation can yield spurious overproduction of black hole seeds. In testing, we found that black holes can form in rapid succession in small regions of space and quickly merge. These spurious bursts of black hole formation are enabled by limited temporal resolution that prevents a newly formed sink particle from heating the surrounding gas enough to prevent or delay subsequent black hole formation. If this sort of runaway black hole formation is allowed to proceed without regulation, it can result in an unphysical amount of mass stored in black holes. As a solution, we implemented two new modules in GASOLINE to identify black holes that formed from gas that should have been heated by feedback from a newly formed black hole and revert these sink particles to their parent gas particles. These modules effectively regulate spurious black hole formation at runtime.

The purpose of the first of the pair of functions, which we call SINKUNFORM, is to identify sink particles that formed too near in time and space to another sink particle that is more bound (i.e., has a deeper gravitational potential). This module uses a tree of sink particles to identify black holes that have just formed. Newly formed particles in GASOLINE are assigned an iOrder of -1, and are easily identified by this attribute. We define SINKUNFORM as a smoothing function: this module will operate once on each item in the smoothing list passed, which in this case is the number of elements in the three of sink particles. Each time SINKUNFORM is called, the n^{th} element of the smoothing list (particle p) is the subject of the operation. If particle p is a newly formed sink, the function iterates over the list of smoothing elements (i.e., the other sink particles in the tree), and evaluates

each element for three qualities. If two sink particles form at the same timestep, they must be separated by a minimum of two softening lengths. Since this is the maximum separation for two sink particles to merge, it should also be the minimum separation for two unique sinks forming concurrently. A sink particle p is considered for deletion if it is newly formed (i.e., has an iOrder of -1), is less than one softening length from another newly formed sink particle, and is less gravitationally bound than this neighbor. If the sink particle p meets all three of these criteria, it is deleted.

Mass conservation requires that the deleted sink particles are replaced by the gas particles from which they formed. The second smoothing function, GASREFORM, carries out this task, matching the iGasOrder of a sink particle with the iOrder of its parent gas particle. GASREFORM operates on a tree of deleted particles, which will include a variety of different particles: newly deleted sinks from SINKUNFORM; gas particles that had been deleted to form these sinks; sinks that were deleted as the result of black hole mergers; and gas particles that were deleted to form other star and sink particles. As GASREFORM iterates over the smoothing list of deleted particles, we check that particle p is a newly formed (and deleted) sink. These particles are again identified by an iOrder of -1; although the iOrder of a deleted particle is modified from its original value ($-$iOrder $-$ 2), this does not transform the iOrders of newly formed particles, as $-\text{iOrder} - 2 = -1 - 2 = -1$. For each such particle p, GASREFORM iterates through the list of smoothing elements that are deleted gas particles. For each gas particle, GASREFORM compares the iOrder of the deleted gas particle to the iGasOrder of the deleted sink. If a sink particle's iGasOrder $= -\text{iOrder} - 2$ of a gas particle, then this is the parent gas particle of the deleted sink. This gas particle is un-deleted, and replaces the deleted sink particle.